

HIGH RESOLUTION CMB POWER SPECTRUM FROM THE COMPLETE ACBAR DATA SET.

C. REICHARDT¹, P.A.R. ADE², J.J. BOCK^{1,3}, J.R. BOND⁴, J.A. BREVIK¹, C.R. CONTALDI⁵, M.D. DAUB⁶, J.T. DEMPSEY⁷, J.H. GOLDSTEIN^{8,9}, W.L. HOLZAPFEL⁶, C.L. KUO^{1,10}, A.E. LANGE^{1,3}, M. LUEKER⁶, M. NEWCOMB¹¹, J.B. PETERSON¹², J. RUHL⁸, M.C. RUNYAN¹, Z. STANISZEWSKI⁸

To appear in ApJ

ABSTRACT

In this paper, we present results from the complete set of cosmic microwave background (CMB) radiation temperature anisotropy observations made with the Arcminute Cosmology Bolometer Array Receiver (ACBAR) operating at 150 GHz. We include new data from the final 2005 observing season, expanding the number of detector-hours by 210% and the sky coverage by 490% over that used for the previous ACBAR release. As a result, the band-power uncertainties have been reduced by more than a factor of two on angular scales encompassing the third to fifth acoustic peaks as well as the damping tail of the CMB power spectrum. The calibration uncertainty has been reduced from 6% to 2.2% in temperature through a direct comparison of the CMB anisotropy measured by ACBAR with that of the dipole-calibrated WMAP3 experiment. The measured power spectrum is consistent with a spatially flat, Λ CDM cosmological model. We see evidence for weak gravitational lensing of the CMB at $> 3\sigma$ significance by comparing the likelihood for the best-fit lensed/unlensed models to the ACBAR+WMAP3 data. On fine angular scales, there is weak evidence (1.7σ) for excess power above the level expected from primary anisotropies. The source of this power cannot be constrained by the ACBAR 150 GHz observations alone; however, if it is the same signal seen at 30 GHz by the CBI and BIMA experiments, then it has a spectrum consistent with the Sunyaev-Zel'dovich effect.

Subject headings: cosmic microwave background — cosmology: observations

1. INTRODUCTION

Observations of the cosmic microwave background (CMB) are among the most powerful and important tests of cosmological theory. Measurements of the angular power spectrum of CMB temperature anisotropies on angular scales $> 10'$ - corresponding to multipoles $\ell \lesssim 1000$ - (Spergel et al. 2006) in conjunction with other cosmological probes (Burles et al. 2001; Cole et al. 2005; Tegmark et al. 2006; Riess et al. 2007) have produced compelling evidence for the Λ CDM cosmological model. At higher multipoles, measurements probe the Silk damping tail of the power spectrum and provide an independent check of the cosmological model.

At smaller angular scales, the primary CMB anisotropies originating at redshift $z = 1100$ are exponentially damped by photon diffusion. This effect, known as Silk damping, makes secondary anisotropies - those induced along the line of sight at lower redshift - increasingly important at higher ℓ . At 150 GHz, for example, the Sunyaev-Zeldovich (SZ) effect is expected to be brighter than the primary CMB anisotropy at $\ell \gtrsim 2500$. The amplitude of the SZ depends sensitively on the amplitude of

the matter perturbations, scaling as σ_8^7 . Measurements of the CMB power spectrum on arcminute scales with sufficient sensitivity thus not only extend tests of the Λ CDM model's ability to accurately predict the features in the power spectrum of primary CMB anisotropy, but also probe the epoch of cluster formation and provide an independent measure of σ_8 .

In this paper we present the final results of observations of CMB temperature anisotropies at 150 GHz with $5'$ resolution, from the ACBAR experiment at South Pole station. Previous measurements of the CMB power spectrum from ACBAR have been presented in Kuo et al. (2004) (hereafter K04) and Kuo et al. (2007) (hereafter K07). In addition, the angular power spectrum on these angular scales has been measured at 30 GHz by CBI (Readhead et al. 2004a), VSA (Dickinson et al. 2004), and BIMA (Dawson et al. 2006), and at 100 and 150 GHz by QUAD (QUAD Collaboration: P. Ade et al. 2007).

To date, the observations at angular scales $< 10'$ have been consistent with predictions of the primary anisotropy based on measurements at larger angular scales, with one exception. Both CBI (Mason et al. 2003; Bond et al.

¹ Observational Cosmology, California Institute of Technology, MS 59-33, Pasadena, CA 91125

² Department of Physics and Astronomy, Cardiff University, CF24 3YB Wales, UK

³ Jet Propulsion Laboratory, 4800 Oak Grove Drive, Pasadena, CA 91109

⁴ Canadian Institute of Theoretical Astrophysics, University of Toronto, Toronto, Ontario, M5S3H8, Canada

⁵ Blackett Laboratory, Imperial College, Prince Consort Road, London, SW7 2AZ, U.K.

⁶ Department of Physics, University of California, Berkeley, CA 94720

⁷ Joint Astronomy Centre, Hilo HI 96720

⁸ Department of Physics, Case Western Reserve University, Cleveland, OH 44106

⁹ Arreté Associates, Arlington, VA 22202

¹⁰ Department of Physics and KIPAC, Stanford University, Stanford, CA 94305

¹¹ Yerkes Observatory, 373 W. Geneva Street, Williams Bay, WI 53191

¹² Department of Physics, Carnegie Mellon University, Pittsburgh, PA 15213

2005) and BIMA (Dawson et al. 2006) observe excess power for $\ell > 2000$ at 30 GHz compared to the predictions of the Λ CDM model. This excess can be explained by the SZ effect if $\sigma_8 \approx 1$, but this value is in tension with the best-fit WMAP3 value of $\sigma_8 \approx 0.7 - 0.8$. The frequency dependence of the excess favors the SZ explanation, but could result from foreground contamination as well (K07). Careful measurements over a broad range of frequencies are needed to provide a definitive answer.

Current estimates of the primordial power spectrum are consistent with the predictions of slow-roll inflation for a nearly scale-invariant spectrum which may also include a small running of the spectral index. Sparked by the modest evidence for negative running in the WMAP first-year data, a number of authors have investigated how existing data sets limit the allowed inflationary scenarios (Peiris et al. 2003; Mukherjee & Wang 2003; Bridle et al. 2003; Leach & Liddle 2003). Small-scale data extend the range over which the primordial power spectrum is measured and yield information about the mechanics of inflation.

This is the third and final ACBAR power spectrum release. The first release in K04 analyzed two fields from the 2001 and 2002 seasons with a conservative field differencing algorithm. The second ACBAR power spectrum, presented by K07, added two more fields from the 2002 season and implemented an improved, undifferenced Lead-Main-Trail (no-LMT) analysis of the dataset. The results presented here improve on the previous work in two ways. First, we include seven additional fields observed in the 2005 Austral winter. These fields triple the total number of detector hours and substantially improve the precision of the band-power estimates. In particular, the new fields were selected to dramatically expand ACBAR’s sky coverage in order to reduce the uncertainties and to improve the multipole resolution on angular scales below $\ell \lesssim 1800$. This angular range covers the third to fifth acoustic peaks, making it especially interesting for constraining cosmological models. Second, we implement a new temperature calibration based on a comparison of CMB fluctuations as measured by ACBAR and the WMAP satellite (Hinshaw et al. 2006). This improved calibration tightens constraints on cosmological models found from the combination of high- ℓ ACBAR band-powers with low- ℓ results from other experiments.

This paper is organized as follows. In § 2 we review the ACBAR instrument and the CMB observation program. The analysis algorithm is explained in § 3. Section § 4 is an overview of the calibration; the details of cross-calibration between WMAP3 and ACBAR are discussed in Appendix A. Information on ACBAR’s beams can be found in § 5. Systematic tests and foreground contamination are discussed in § 6. We present the band-power results in § 7, including a discussion of the scientific interpretation. The ACBAR band powers are combined with the results of other experiments to place constraints on the parameters of cosmological models in § 8. In § 9, we summarize the main results of this paper.

2. THE INSTRUMENT AND OBSERVATIONS

The ACBAR receiver was designed to take advantage of the excellent observing conditions at the

South Pole to make extremely deep maps of CMB anisotropies (Runyan et al. 2003). It observes from the Viper telescope, a 2.1m off-axis Gregorian with a beam size of $5'$ at 150 GHz. The beams are swept across the sky at near-constant elevation by the motion of an actuated flat tertiary mirror.

The receiver contains 16 optically active bolometers cooled to 240 mK by a three-stage He^3 - He^3 - He^4 sorption refrigerator. The results reported here are derived from the 150 GHz detectors: there were 4-150 GHz bolometers in 2001, 8 in 2002 and 2004, and 16 in 2005. The detectors were background limited at 150 GHz with a sensitivity of approximately $340 \mu\text{K}\sqrt{\text{s}}$.

In total, ACBAR observed 10 independent CMB fields, detailed in Table 1. The power spectrum derived from portions of four fields, CMB2/4, CMB5, CMB6, and CMB7 was reported in K07. Since then, we have completed the analysis of six new fields observed in 2005 as well as additional observations of the original four fields. Details of the instrument configuration and performance in the 2001 and 2002 seasons are given in Runyan et al. (2003), while additional details of the CMB observations, data reduction procedures, and beam maps can be found in K04 and K07.

3. UN-DIFFERENCED POWER SPECTRUM ANALYSIS

Following the conventions of the previous data releases, the band-powers \mathbf{q} are reported in units of μK^2 , and are used to parameterize the power spectrum according to

$$\ell(\ell+1)C_\ell/2\pi \equiv \mathcal{D}_\ell = \sum_B q_B \chi_{B\ell}, \quad (1)$$

where $\chi_{B\ell}$ are tophat functions; $\chi_{B\ell} = 1$ for $\ell \in B$, and $\chi_{B\ell} = 0$ for $\ell \notin B$. The ACBAR observations were carried out in a *lead-main-trail* (LMT) pattern. Originally, the three fields were differenced according to the formula $M - (L + T)/2$ in order to remove time-dependent chopper synchronous offsets. In K07, this conservative strategy was shown to be unnecessary and an un-differenced analysis algorithm was presented. We continued to observe in a lead-trail or LMT pattern in 2005 in order to produce maps wider than the maximum range ($\sim 3^\circ$) of the chopping tertiary mirror. The un-differenced analysis presented in K07, and used for this paper’s analysis, is outlined below with any differences in the application to the 2005 data set highlighted.

Let d_α be a measurement of the CMB temperature at pixel α . The data vector can be represented as the sum of the signal, noise and chopper synchronous offsets: $d_\alpha = s_\alpha + n_\alpha + o_\alpha$. For example, although the chopping mirror moves the beams at nearly-constant elevation, the slight residual atmospheric gradient produces a chopper synchronous signal o_α which is an approximately quadratic function of chopper angle. To remove these offsets, the data from each chopper sweep are filtered with the “corrupted mode projection” matrix $\mathbf{\Pi}$ to produce the cleaned time stream $\mathbf{d} \equiv \mathbf{\Pi}\mathbf{d}$.

The $\mathbf{\Pi}$ matrix projects out a third to tenth order polynomial which suppresses large angular scale chopper offsets. The order of the polynomial removed depends on the amplitude of atmosphere-induced cross-channel correlations. As described in K07, small angular scale offsets can be removed by subtracting an “average” chopper function.

TABLE 1
CMB FIELDS

Field	RA (deg)	dec (deg)	Area (deg ²)	Year	# of detectors	Detector hours
CMB2(CMB4)	73.963	-46.268	26(17)	2001(2002)	4(8)	2.0k(1.1k)
CMB5	43.371	-54.836	28	2002(2005)	8(16)	13.2k(10.6k)
CMB6	32.693	-50.983	23	2002	8	2.8k
CMB7(ext*)	338.805	-48.600	28(107)	2002(2005)	8(16)	3.4k(12.4k)
CMB8	338.805	-48.600	61	2005	16	17.1k
CMB9*	359.818	-53.135	93	2005	16	4.0k
CMB10*	19.544	-53.171	93	2005	16	3.6k
CMB11*	339.910	-64.178	91	2005	16	4.9k
CMB12*	21.849	-64.197	92	2005	16	2.7k
CMB13*	43.732	-59.871	78	2005	16	7.6k

Note. — The central coordinates and size of each CMB field observed by ACBAR. The sixth column gives the number of 150 GHz detectors. The last column gives the detector integration time for each field after cuts. The detector sensitivity was comparable (within $\sim 10\%$) between 2002 and 2005. The six largest fields (marked with a *) are used in the calibration to WMAP. Note that the 2005 observations extended the declination range of the CMB7 field, leading to the combined field CMB7ext. CMB2(CMB4) and CMB8 also partially overlap, but are analyzed separately for computational reasons. Approximately 1/4 of the CMB2(CMB4) scans have been discarded to eliminate the overlapping coverage. The listed numbers reflect this loss.

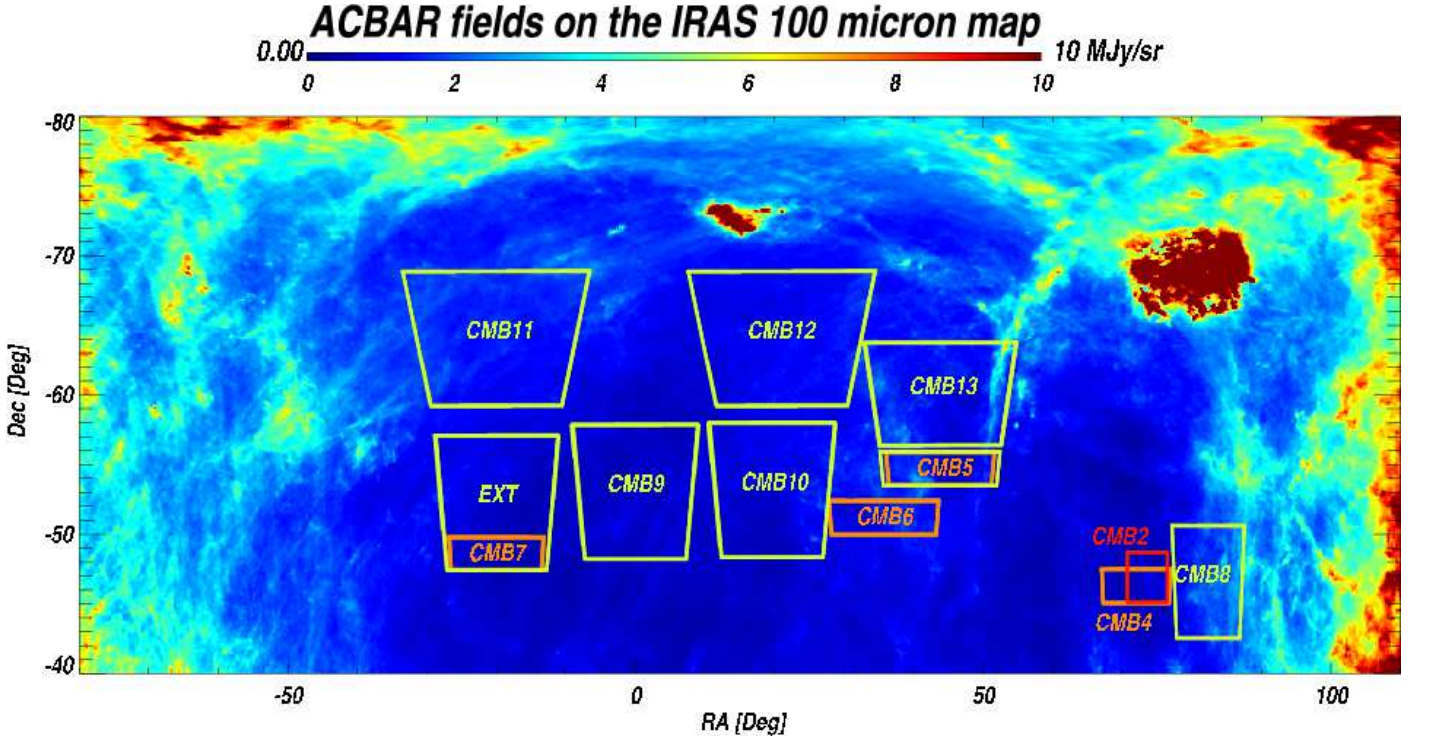


FIG. 1.— The ACBAR fields overlaid on the IRAS dust map. The position of each field is plotted and labeled with the field name. The color coding indicates the year in which the observations occurred: red \equiv 2001, orange \equiv 2002, and yellow \equiv 2005. The bulk of the 2005 season was targeted at large, comparatively shallow fields, increasing the total sky coverage by a factor of six. The fields are plotted on top of the $100\ \mu\text{m}$ IRAS dust map (Schlegel et al. 1998). Each field has been targeted at the “Southern hole”, a region of low dust emission visible from the South Pole. The CMB8 field (lower right corner) was targeted at the deep region of the B03 experiment as an alternative calibration path to the WMAP cross-calibration used for the results presented here.

For 2002 data, we removed a chopper synchronous offset from each data strip where the amplitude of the offset at each sample in the strip is free to vary quadratically with elevation in the map. The large fields observed in 2005 have up to four times the dec range of the fields observed in 2001 and 2002 ($\sim 10^\circ$ vs. $\sim 2.5^\circ$). For 2005 data, we

allow the offset to vary from a third to fifth order polynomial depending on the extent of the map in declination. A zeroth order polynomial in elevation removes the average chopper function and the higher order terms effectively act as a high-pass filter on changes in the offset as a function of time or elevation. This anisotropic filtering removes offset-

corrupted modes while preserving most of the uncorrupted modes for the power spectrum analysis. The loss of information at high- ℓ is small; the removed modes account for only a few percent of the total degrees of freedom of the data.

The corrupted mode projection matrix Π can be represented as the product of two matrices, $\Pi \equiv \Pi_2 \Pi_1$. The operator Π_1 is the original Π matrix referenced in K04 which adaptively removes polynomial modes in RA. The additional operator Π_2 removes modes in dec independently for each of the lead, main, and trail fields and can be further decomposed into the product $\Pi_2 = \Pi_2^{Poly} \Pi_2^{LPF}$. The operator Π_2^{Poly} performs the aforementioned polynomial projection in dec to remove small-scale chopper offsets. The second operator Π_2^{LPF} imposes a low-pass filter (LPF) $\ell < 3200$ on each dec strip. The dec strips are perpendicular to the scan direction; the timestreams have always had a LPF applied in the scan direction. The pixelation used when estimating the power spectrum is too large to resolve all of the noise power (at ℓ up to 10,800), causing out-of-band noise to be aliased into the signal band ($\ell < 3000$) if a LPF is not applied. Eliminating this high-frequency noise reduces the contribution of instrumental noise to the reported band-powers.

Using the pointing model, the cleaned timestreams are coadded to create a map:

$$\Delta = \mathbf{L} \mathbf{d}.$$

The noise covariance matrix of the map can be represented as

$$\mathbf{C}_N = \mathbf{L} \langle \mathbf{n} \mathbf{n}^t \rangle \mathbf{L}^t.$$

where \mathbf{n} is the timestream noise. The noise matrix is diagonalized as part of applying a high signal-to-noise transformation to the data. Eliminating modes with insignificant information content reduces the computational requirements of later steps in the analysis.

In order to apply the iterative quadratic band-power estimator, we need to know the partial derivative $\frac{\partial \mathbf{C}_T}{\partial q_B}$ of the theory covariance matrix \mathbf{C}_T with respect to each band-power q_B . The theory matrix can be calculated by considering the effects of the filtering on the raw sky signal. The signal timestream s_α is the convolution of the true temperature map $\mathfrak{T}(\mathbf{r})$ with the instrumental beam function $B_\alpha(\mathbf{r})$

$$s_\alpha = \int d^2 r \mathfrak{T}(\mathbf{r}) B_\alpha(\mathbf{r}).$$

The signal component of the coadded map will be $\Delta^{\text{sig}} = \mathbf{L} \mathbf{s}$ or

$$\Delta_i^{\text{sig}} = \int d^2 r F_i(\mathbf{r}) \mathfrak{T}(\mathbf{r}),$$

where we have defined the pixel-beam filter function F_i

$$F_i(\mathbf{r}) = \sum_\alpha L_{i\alpha} B_\alpha(\mathbf{r}).$$

The theory covariance matrix can be calculated in the flat sky case to be

$$\begin{aligned} C_{T\{ij\}} &\equiv \langle \Delta_i \Delta_j \rangle^{\text{sig}} = \iint d^2 r d^2 r' F_i(\mathbf{r}) F_j(\mathbf{r}') \langle \mathfrak{T}(\mathbf{r}) \mathfrak{T}(\mathbf{r}') \rangle \\ &= \iint d^2 r d^2 r' F_i(\mathbf{r}) F_j(\mathbf{r}') \int \frac{d^2 \ell}{(2\pi)^2} C_\ell \cdot e^{i\ell \cdot (\mathbf{r} - \mathbf{r}')} \end{aligned}$$

$$= \int \frac{d^2 \ell}{(2\pi)^2} C_\ell \cdot \tilde{F}_i^*(\mathbf{l}) \tilde{F}_j(\mathbf{l}), \quad (2)$$

where $\tilde{F}_i(\mathbf{l})$ is the Fourier transform of the pixel-beam filter function. The partial derivative of the theory matrix can be calculated in a straightforward manner from equations 1 and 2.

This algorithm does not require the instrument beams to remain constant. The actual ACBAR beam sizes vary slightly with chopper angle (Runyan et al. 2003). The measured beam variations can be fit to a semi-analytic function as described in K04 to create a more accurate representation of the true beam shape across the map. We use the corrected beam sizes when removing point sources. In K04 and K07, we found that the differences in the power spectra from using the map-averaged beam or exact beam for each pixel were negligible. For the band-powers reported in Table 3, an averaged beam is used for the entire map.

As in K07, we calculate the full two dimensional noise correlation matrix directly from the time stream data without using Fourier transforms. All the numerical calculations are performed on the National Energy Research Scientific Computing Center (NERSC) IBM SP RS/6000. The evaluation of the Fourier transform of $F_i(\mathbf{r})$ is the most computationally expensive step of this analysis. We use an iterative quadratic estimator to find the maximum likelihood band-powers (Bond et al. 1998). The resulting band-powers are presented in Table 3 and Figure 5.

4. CALIBRATION

We derive the absolute calibration of ACBAR by directly comparing the 2005 ACBAR maps to the WMAP3 V and W-band temperature maps (Hinshaw et al. 2006). We pass the WMAP3 maps through a simulated version of the ACBAR pipeline to ensure equivalent filtering. Cross-spectra are calculated for each field. The ratios of the cross-spectra are used to measure the relative calibration after being corrected for the respective instrumental beam functions. Results for ACBAR's six largest fields (approximately 600 deg^2 in area) are combined to achieve an accuracy of 2.17% for the 2005 data.

The 2005 calibration is transferred to 2001 and 2002 through a comparison of power spectra for overlapping regions observed by ACBAR in each year. The CMB5 field is used to extend the calibration of the 2005 season to the 2002 data. The CMB5 calibration is carried to other fields observed in 2002 by daily observations of the flux of RCW38. The calibration of the CMB4 field (observed in 2002) then is transferred to the 70% overlapping CMB2 field (observed in 2001). According to the new calibration, results from the RCW38-based calibration used for the 2002 data in K07 need to be multiplied by 0.973 ± 0.032 . Including the year-to-year calibration uncertainty, the final calibration has an uncertainty of 2.23% in CMB temperature units (4.5% in power). Additional details of this procedure are discussed in Appendix A.

5. BEAM DETERMINATION

The beams are well-described by a symmetric Gaussian, with their main-lobe FWHM determined to 2.6% by continuous measurements of the images of bright quasars lo-

cated in the CMB fields. The beam sidelobes were measured to the level of 30 dB with observations of Venus made in 2002. Venus is extremely bright at millimeter wavelengths and with a diameter of $\lesssim 1'$, is much smaller than ACBAR's beam size. However, there are extended periods during which ACBAR was unable to observe Venus. ACBAR observed RCW38, a bright HII region in the galactic plane, every day. We compare deep, coadded observations of RCW38 to constrain the temporal variability of the beam sidelobes when Venus was unavailable. The complex structure surrounding RCW38 makes it difficult to directly recover the beam shape $B(\mathbf{r})$. Instead, we monitor ratios of the beam-smoothed RCW38 maps $\int d^2r S^{RCW38}(\mathbf{r})B(\mathbf{r})$. Any observed differences in the maps would indicate a change to the instrumental beam function as the morphology of RCW38's emission S^{RCW38} is expected to be constant. We set an upper limit on the possible temporal variations in the map and use this to constrain temporal variations in the beam function. The estimated band-power uncertainty from the beam function is comparable to the overall calibration uncertainty and is plotted in Figure 2.

6. SYSTEMATIC UNCERTAINTIES AND FOREGROUNDS

6.1. Jackknife Tests

We performed a series of tests to search for and constrain potential systematic errors in the power spectrum results. As described in K04, the data can be divided into two halves based on whether the chopping mirror is moving to the left or right. The “left minus right” jackknife is a sensitive test for errors in the transfer function correction, microphonic vibrations excited by the chopper motion, or the effects of wind direction. Maps with bright sources such as RCW38 can provide particularly sensitive tests of the transfer function (see Runyan et al. (2003) for a description of ACBAR's transfer functions). Similarly, the data can be split based on the time that the observation occurred. A non-zero signal could be produced in the “first half minus second half” jackknife by variation in the calibration, pointing, beam and sidelobe, or any other time dependent variations in the instrument. In addition, the band-powers of each jackknife constrain the mis-estimation of noise during that period.

We applied the left-right jackknife to the 2005 CMB data and found the band-powers were inconsistent with zero at 2.5σ at high- ℓ ($\ell > 2100$). We reran a set of left-right jackknives dropping individual channels, and found that two channels stood out. With both channels excluded, the discrepancy in the left-right jackknife band-powers disappeared. We were unable to find evidence for unusual microphonic lines or transfer functions in the two problematic channels, but hypothesize that these two channels have subtle microphonic response in the signal bandwidth that are detectable only in a deep integration. Both channels are excluded from the 2005 data for all results reported in this paper.

We apply the first-second half jackknife test to the joint CMB power spectrum with the exclusion of the bad channels from the 2005 data. The power spectrum of the chronologically differenced maps is compared to the band-powers of a set of Monte Carlo realizations of simulated difference maps in order to account for a number of effects

such as the small filtering differences due to different scan patterns and the temporal uncertainty in the beam sidelobes (see §5). We find that the jackknife band-powers are consistent with the predictions of the Monte Carlo above $\ell = 400$. There is a 4σ residual of $\sim 15 \mu K^2$ in the first bin. Because the combined statistical and cosmic variance uncertainty in this bin is a factor of six larger, we assume that the band-power estimate will not be significantly biased.

We also perform the left-right jackknife on the joint CMB power spectrum found from the complete data set. The results are consistent with zero for $\ell > 900$. Statistically, the probability to exceed the measured χ^2 for $\ell > 900$ is 15%. The results are inconsistent with zero at a very low ($\sim 4 \mu K^2$) level (Fig. 3) on larger angular scales. This residual could be due to a small noise mis-estimate at low- ℓ , possibly caused by neglected atmospheric correlations. The jackknife failure of $\sim 4 \mu K^2$ is much smaller than the band-power uncertainties ($90 - 300 \mu K^2$) in these ℓ -bins which are dominated by cosmic variance. The first-second half jackknife is insensitive to discrepancies of this magnitude due to the greater uncertainties introduced by small pointing and filtering differences. We conclude that the complete ACBAR data set shows no significant residuals in the jackknife tests and we expect no significant systematic contamination of the resulting power spectrum.

6.2. Foregrounds

The potential contribution of foreground emission must be considered in the interpretation of CMB temperature anisotropies. There are three foregrounds with significant emission at 150 GHz on the relevant angular scales: galactic dust, extragalactic radio sources, and dusty protogalaxies. As an effectively single-frequency instrument, ACBAR depends on data from other experiments to construct and constrain foreground models. We use the methodology described in K04 to remove templates for radio sources and dust emission from the CMB maps without making assumptions about their flux. We believe the residual foreground emission does not significantly impact the power spectrum for $\ell < 2400$.

We remove modes from the CMB maps corresponding to radio sources in the the 4.85 GHz Parkes-MIT-NRAO (PMN) survey (Wright et al. 1994). Of the 1601 PMN sources with a flux greater than 40 mJy that lie in the ACBAR fields, we detect 37 sources including the guiding quasars at greater than 3σ with the application of an optimal matched filter. There are less than 2.2 false detections expected with this detection threshold. The measurement errors are estimated through sampling the distribution of pixels in a set of 100 Monte Carlo realizations of the CMB+noise for each field. Table 2 lists the parameters of the detected PMN sources. Except for the sources detected at 150 GHz, removing the PMN point sources does not significantly affect the bandpowers.

It is possible that faint sources, undetected at 150 GHz, could contribute to the observed bandpowers at some level. We parameterize the contributions as

$$\mathcal{D}_\ell^{\text{src}} = q_{\text{src}} \left(\frac{\ell}{2600} \right)^2 \mu K^2 \quad (3)$$

which is appropriate for unclustered point sources. To estimate this contribution, we compare the 150 GHz ACBAR point source number counts to the model in

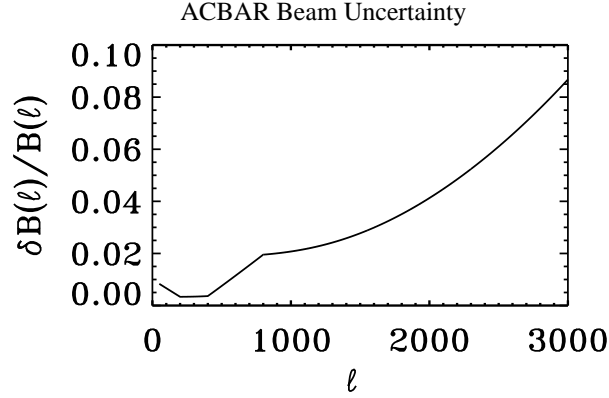


FIG. 2.— ACBAR Beam Uncertainty. The 1σ envelope for uncertainty in the ACBAR beam function B_ℓ . The increasing uncertainty above $\ell = 1000$ reflects the 2.6% uncertainty in the fitted Gaussian FWHMs. The behavior at $\ell < 1000$ is a combination of the uncertainty in the measured sidelobes and the the calibration method ‘pinning’ the transfer function for $\ell \in [256, 512]$.

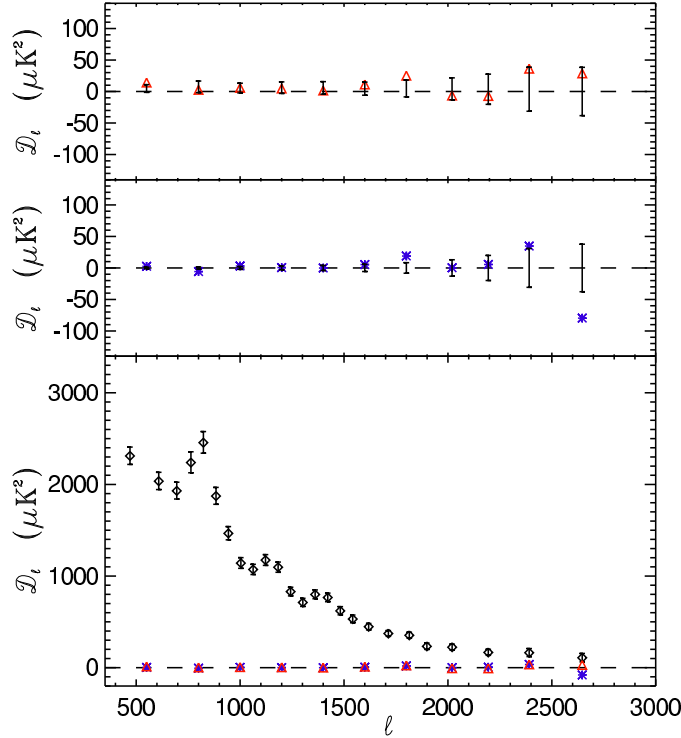


FIG. 3.— Systematic tests performed on the ACBAR data. *Top*: Power spectrum (blue star) for differenced maps from the first half of the season and second half of the season for each field, compared to the results of Monte Carlo simulations (error bars). *Middle*: Power spectrum (red triangle) derived from difference maps of the left- and right-going chopper sweeps for all ten fields. *Bottom*: The undifferenced band-powers from Table 3 (black diamonds) compared to both jackknife power spectra: the left-right jackknife (blue star) and first half-second half jackknife (red triangle).

White & Majumdar (2004) based on WMAP Q-band data,

$$\frac{dN}{dS_\nu} = \frac{80 \text{ deg}^{-2}}{1 \text{ mJy}} \left(\frac{S_\nu}{1 \text{ mJy}} \right)^{-2.3},$$

to constrain the residual power contribution at 150 GHz. Following the convention in that work, the spectral dependence of the fluxes is parameterized as $S_\nu \propto \nu^\beta$. We estimate β in two ways. Using the PMN sources detected at 150 GHz, the number counts in a logarithmic flux bin, n_B^{obs} , are compared to the predicted number counts from the

same population of sources with a given β , $n_B^{(\beta)} + n_B^{noise}$. Here, $n_B^{(\beta)}$ is the modeled number counts and n_B^{noise} is the expected number of false detections due to ACBAR’s measurement error. The number counts are assumed to follow a Poissonian distribution. Sources with estimated measurement errors greater than 140 mJy in the ACBAR maps are cut to reduce the n_B^{noise} term. The model number counts $n_B^{(\beta)}$ are scaled by $(N_{tot} - N_{cut})/N_{tot}$ to compensate. All other sources with measured amplitudes greater than 350 mJy at 150 GHz are included in the calculation without consideration of the signal-to-noise. For the

source counts at 150 GHz to be due to the same population found by WMAP would require a uniform spectral index of $\beta = 0.16 \pm 0.16$. However, this small sample selected for high flux at 150 GHz is heavily biased toward sources with flat or rising spectra. We increase ACBAR's sensitivity to dimmer sources by binning all sources within a given PMN flux range, and look at the ratio of the average flux at GHz to the average flux at 4.85 GHz within each bin. We find the ratio ($S_{150}/S_{4.85}$) increases with PMN flux from 0.07 for sources below 400 mJy to 0.41 for sources above 1600 mJy at 4.85 GHz. This would be consistent with a flux-dependent spectral index with which dimmer objects have a falling spectrum. We estimate the band-power contributions from radio sources with this information. The estimate depends sensitively on the extrapolation of the 40 mJy flux cutoff in the 4.85 GHz PMN catalog to 150 GHz. Based on the observed flux ratios for PMN sources with $S_{4.85} < 400$ mJy, we conservatively assume $S_{150}/S_{4.85} = 0.1$ for a flux cutoff at 4 mJy at 150 GHz. This flux ratio corresponds to a spectral index of $\beta = -0.67$, well below the $\beta = 0.16 \pm 0.16$ estimated from the ACBAR detected sources and the WMAP Q-band source model. Estimating the radio source band-power contribution at 150 GHz with a flux cutoff of 4 mJy gives $q_{\text{src}}^{\text{radio}} = 2.2$. At this level, the residual contribution from radio sources will be negligible in the ACBAR data.

The ACBAR fields are positioned in the ‘‘Southern Hole,’’ a region of exceptionally low Galactic dust emission (Figure 1). Finkbeiner et al. (1999) (FDS99) constructed a multi-component dust model that predicts thermal emission at CMB frequencies from the combined observations of IRAS, COBE/DIRBE, and COBE/FIRAS. Taking into account the ACBAR filtering, the FDS99 model¹³ predicts a RMS dust signal at the μK level primarily on large angular scales. The ACBAR maps can be decomposed as the sum of the CMB and dust signals $T_{\text{CMB}} + \xi T_{\text{FDS}}$. The dust amplitude parameter ξ is predicted to equal unity by the FDS99 model. The ACBAR maps are cross-correlated with the dust templates T_{FDS} to calculate the amplitude in each field. The errors are estimated by applying the same procedure to 100 CMB+noise map realizations for each field. The uncertainty in ξ is dominated by CMB fluctuations. The best-fit amplitude from combining all the fields is $\xi = 0.1 \pm 0.5$. The estimated amplitudes of the individual fields are shown in Figure 4. The reduced χ^2 of the measured amplitudes ξ s of the eight fields analyzed is 0.75 for the no-dust assumption of $\langle \xi \rangle = 0$ and increases to $\chi^2 = 1.12$ for the FDS99 model amplitude of $\langle \xi \rangle = 1$. Therefore, the ACBAR data slightly favor a lower amplitude than predicted by the FDS99 model. The dust signal is not detectable in any of the ACBAR fields, and removing the dust template has a negligible impact on the measured power spectrum.

Dusty IR galaxies are the third and least constrained potential foreground in the ACBAR fields. This population of high-redshift, star-forming galaxies has been studied by several experiments at higher frequencies (Coppin et al. 2006; Laurent et al. 2005; Maloney et al. 2005; Greve et al. 2004). However, as discussed in K07, extrapolating the expected signal to 150 GHz remains highly

uncertain, and there remain significant uncertainties in the number counts $\frac{dN}{dS}$ and spatial clustering of the sources. The frequency dependence can be empirically determined by comparing the measured number counts in overlapping fields observed at different frequencies. This comparison has been done with MAMBO (1.2 mm) and SCUBA (850 μm), leading to spectral dependence of $S_\nu \propto \nu^{2.65}$ (Greve et al. 2004). However, the Bolocam data suggest a steeper source spectrum, with fewer sources found at 1.1 mm (Laurent et al. 2005; Maloney et al. 2005). Fitting to Figure 15 in Laurent et al. (2005), we estimate the spectral dependence to be $S_\nu \propto \nu^4$. The uncertainty in the spectral dependence significantly affects the extrapolation of the flux of dusty galaxies to 150 GHz. We use estimates of the source number counts from the SHADES survey (Coppin et al. 2006) and Bolocam Lockman Hole Survey (Maloney et al. 2005). We apply the formulas in Scott & White (1999) to estimate the expected power spectrum for the source number counts, ignoring the clustering terms. In this limit, \mathcal{D}_ℓ will have the form in eq. 3. Scaling the results to 150 GHz with the MAMBO/SCUBA prescription of $S_\nu \propto \nu^{2.65}$ leads to an estimated contribution of $q_{\text{src}}^{\text{dusty}} = 17 - 29$. A third method of estimating the index used nearby galaxy data (Knox et al. 2004) to obtain $S_\nu \sim \nu^{2.6 \pm 0.3}$. Combining the median index with earlier SCUBA data fit by two power laws in S from (Borys et al. 2003), we find an excess of $22 \mu\text{K}^2$ at $\ell = 2600$, within that range. This level is only a factor of two smaller than the instrumental noise of ACBAR and might influence the interpretation of high- ℓ band-powers. If we instead use the Bolocam/SCUBA spectral index, the estimated contribution is only $q_{\text{src}}^{\text{dusty}} \sim 2 - 6$. For the results presented in this work, we tentatively assume that dusty proto-galaxies do not contribute significant power at high- ℓ . The implications of relaxing this assumption for cosmological parameter estimation are explored in § 8.3.

7. RESULTS AND DISCUSSIONS

7.1. Power Spectrum

The power spectrum presented in Figure 5 is produced by the application of the analysis algorithm outlined in § 3 to ACBAR data from the 2001, 2002 and 2005 austral winters. The resulting power spectrum is compared to the WMAP3 and B03 spectra in Figure 6. The zero-curvature, ΛCDM ‘‘ACBAR+WMAP3’’ best fit model is shown in each figure for reference. The decorrelated band-powers are tabulated in Table 3. Our choice of the decorrelation transformations follows Tegmark (1997). The band-powers can be compared to a theoretical model using the window functions (Knox 1999). As in K04, we sample the likelihood function $\mathcal{L}(\Delta) = \frac{1}{\sqrt{C}} e^{-(\Delta^t C^{-1} \Delta)/2}$ near the maximum and fit the results with offset lognormal functions (Bond et al. 2000). The fit parameters σ, \mathbf{x} are listed in Table 3 as well. The band-powers, likelihood fit parameters, and window functions are available for download from the ACBAR website¹⁴.

The ACBAR data extend the measurement of the temperature anisotropies well into the damping tail with $S/N > 5$ for $\ell \lesssim 2300$. The fourth and fifth acous-

¹³ We use the default model 8 of FDS99.

¹⁴ <http://cosmology.berkeley.edu/group/swlh/acbar/index.html>

TABLE 2
MILLIMETER BRIGHT PMN SOURCES

Source Name/Position	Field	$S_{4.85}$ (mJy)	S_{150} (mJy)	$\alpha_{150/4.85}$
PMN J0455-4616* [◦]	CMB2	1653	2898 ± 60	0.16
PMN J0439-4522	CMB2	634	383 ± 73	-0.15
PMN J0451-4653	CMB2	541	360 ± 58	-0.12
PMN J0253-5441* [◦]	CMB5	1193	1277 ± 63	0.02
PMN J0223-5347	CMB5	397	176 ± 28	-0.24
PMN J0229-5403	CMB5	242	147 ± 18	-0.14
PMN J0210-5101* [◦]	CMB6	3198	1268 ± 86	-0.27
PMN J2207-5346 [◦]	CMB7ext	1410	381 ± 67	-0.38
PMN J2235-4835 [◦]	CMB7ext	1104	1529 ± 76	0.09
PMN J2239-5701 [◦]	CMB7ext	1063	501 ± 67	-0.22
PMN J2246-5607	CMB7ext	618	386 ± 49	-0.14
PMN J2309-5703	CMB7ext	56	257 ± 79	0.44
PMN J0519-4546a [◦]	CMB8	15827	1393 ± 103	-0.92*
PMN J0519-4546b [◦]	CMB8	14551	1163 ± 87	-0.92*
PMN J0538-4405* [◦]	CMB8	4805	7209 ± 89	0.12
PMN J0515-4556 [◦]	CMB8	990	680 ± 98	-0.11
PMN J0526-4830	CMB8	425	82 ± 27	-0.48
PMN J0525-4318	CMB8	217	99 ± 27	-0.23
PMN J0531-4827	CMB8	142	96 ± 27	-0.11
PMN J2357-5311 [◦]	CMB9	1782	347 ± 50	-0.48
PMN J2336-5236	CMB9	1588	233 ± 56	-0.56
PMN J2334-5251	CMB9	557	432 ± 56	-0.07
PMN J0018-4929	CMB9	142	178 ± 56	0.07
PMN J0026-5244	CMB9	40	192 ± 63	0.46
PMN J0050-5738 [◦]	CMB10	1338	773 ± 104	-0.16
PMN J0058-5659 [◦]	CMB10	739	514 ± 60	-0.11
PMN J0133-5159 [◦]	CMB10	672	248 ± 63	-0.29
PMN J0124-5113 [◦]	CMB10	308	335 ± 49	0.02
PMN J2208-6404	CMB11	53	136 ± 44	0.27
PMN J0103-6438	CMB12	395	268 ± 63	-0.11
PMN J0144-6421	CMB12	152	184 ± 60	0.06
PMN J0303-6211 [◦]	CMB13	1862	429 ± 63	-0.43
PMN J0309-6058 [◦]	CMB13	1103	604 ± 81	-0.18
PMN J0251-6000	CMB13	433	189 ± 34	-0.24
PMN J0236-6136	CMB13	406	365 ± 35	-0.03
PMN J0257-6112	CMB13	178	104 ± 35	-0.16
PMN J0231-6036	CMB13	174	105 ± 35	-0.15

Note. — These sources from the PMN 4.85 GHz catalog are detected at $> 3.0\sigma$ significance with ACBAR, corresponding to a false detection rate of < 2.2 . The fluxes at 4.85 GHz ($S_{4.85}$, from Wright et al. (1994)) and 150 GHz (S_{150} , measured by ACBAR) are given. For ACBAR, the flux conversion factor is $1 \mu K_{CMB} = 0.9$ mJy. The spectral index α is defined as $S_\nu \propto \nu^\alpha$. The flux of some of these sources varied by up to 50% between years; this variability is not reflected in the estimated errors. The central guiding quasars (one in each of the 5 deeper fields) are marked with asterisks (*). These sources, as well as the undetected PMN sources, are projected out from the data using the methods described by K04 and do not contribute to the power spectrum measurements reported in this paper. The brightest sources are marked with circles ([◦]) and are removed from the maps in a beam-independent method. Note that PMN J0519-4546a/b are within one beam width of each other and are not separately resolved by ACBAR. As a result, the listed α for PMN J0519-4546a/b is estimated from the sum of the fluxes at 4.85 GHz and the mean of the fluxes at 150 GHz.

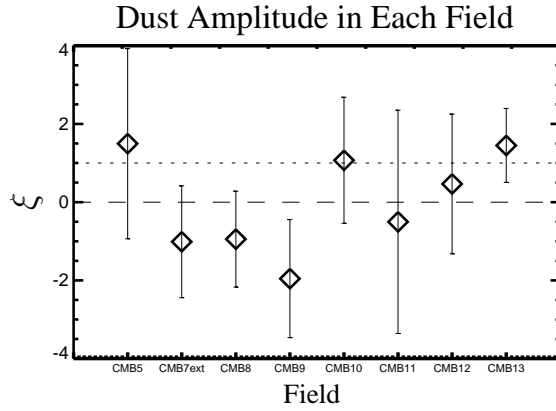


FIG. 4.— Dust emission is not detected in the ACBAR fields. Parameterizing the dust signal as $T_{CMB} + \xi T_{FDS}$, a suite of Monte Carlo realizations of maps of CMB and noise is used to estimate the uncertainty in ξ . We find the upper limits in each field to be consistent with the FDS99 model ($\xi = 1$), but the data somewhat favor a lower dust amplitude. The reduced χ^2 of the measured amplitudes ξ s is 0.75 under the assumption that $\langle \xi \rangle = 0$ (the dashed line). The reduced χ^2 for the FDS99 model with $\langle \xi \rangle = 1$ is 1.12 (the dotted line).

tic peaks are detected for the first time in the ACBAR band-powers, providing additional support for the coherent origin of anisotropy (Albrecht et al. 1996). The position of the third acoustic peak is consistent with previous detections of the feature by CBI (Readhead et al. 2004a), B03 (Jones et al. 2006), ACBAR (K07), and QUaD (QUaD Collaboration: P. Ade et al. 2007). The ACBAR band-powers are in excellent agreement with the cosmological models defined at larger angular scales. The probability to exceed the reduced χ^2 between the ACBAR band-powers and the WMAP3 only best-fit Λ CDM model is 16%. This probability increases to 21% with the removal of a flat SZ excess at high- ℓ as discussed in §7.2. This is a powerful confirmation of our understanding of the physics behind the CMB temperature anisotropies.

7.2. Anisotropies at $\ell > 2000$

Several theoretical calculations (Cooray et al. 2000; Komatsu & Seljak 2002) and hydrodynamical simulations (Bond et al. 2005; White et al. 2002) suggest that the thermal Sunyaev-Zel'dovich effect power spectrum will exceed that of the primary CMB temperature anisotropies for $\ell \gtrsim 2500$ at 150 GHz. The amplitude of the SZ power spectrum is closely related to the amplitude of matter perturbations which is commonly parameterized as σ_8 ; the SZ power spectrum is expected to scale as σ_8^2 (Zhang et al. 2002). To a lesser extent, the level of the SZ will also depend on details of cluster gas physics and thermal history. The non-relativistic thermal SZ (ΔT_{SZ}) has a unique frequency dependence

$$\frac{\Delta T_{SZ}}{T_{CMB}} = y \left(x \frac{e^x + 1}{e^x - 1} - 4 \right), \quad (4)$$

where $x = \frac{h\nu}{kT_{CMB}} = \nu/56.8 \text{ GHz}$. The variable y is the Compton parameter and is proportional to the integrated electron pressure along the line of sight. The CBI extended mosaic observations (Readhead et al. 2004a) detected more power above $\ell = 2000$ than is expected from primary CMB anisotropies. The excess may be the first detection of the SZ power spectrum (Mason et al. 2003; Readhead et al. 2004a; Bond et al. 2005). However, there are alternative explanations for the observed power ranging from an unresolved population of low-flux radio sources

to non-standard inflationary models (Cooray & Melchiorri 2002; Griffiths et al. 2003; Subramanian et al. 2003) that produce higher than expected CMB anisotropy power at small angular scales. The frequency dependence of the excess can be exploited to help discriminate between the SZ and other potential explanations for observed power.

The ACBAR band-powers reported in this paper are slightly larger at $\ell > 2000$ than expected for the “ACBAR+WMAP3” best fit model. We subtract the predicted band-powers at $\ell > 1950$ from the measured band-powers in Table 3 and fit the residuals to a flat spectrum. We find an excess of $34 \pm 20 \mu K^2$ for a flat band from $1950 < \ell < 3000$. This excess could have the same source as the excess reported by CBI at 30 GHz, although it is certainly possible that the excess power in each experiment is dominated by a unique foreground. If we assume the signals in both experiments have the same source, the ACBAR excess at 150 GHz can be compared to the CBI excess measured at 30 GHz to place constraints on the frequency spectrum of the source. The ACBAR+WMAP3 model band-powers are subtracted from the measured band-powers of each experiment at $\ell > 1950$. We parameterize the excess at the two frequencies as $P_{30} = \alpha P_{150}$ and sample the likelihood surface for $\alpha \in [0, 10]$ and $P_{150} \in [0, 300] \mu K^2$. The beam uncertainty and the calibration error for both experiments is taken into account by Monte Carlo techniques. The likelihood function is averaged over 1000 realizations under the assumption that each of the errors has a normal distribution. The resultant likelihood function (after P_{150} is marginalized) is shown in Figure 7. Given the ACBAR and CBI frequency bands, we expect $\alpha = 4.3$ for the SZ effect. If the excess is due to primary CMB anisotropies, we expect $\alpha = 1$. We conclude that it is 6 times more likely that the excess seen by CBI and ACBAR is caused by the thermal SZ effect than a primordial source. We expect the contribution of radio sources to CMB power to be at least a factor of ten higher at 30 GHz than at 150 GHz ($\alpha \leq 0.1$). Because of the relatively weak detection of excess power by ACBAR, radio sources are only slightly disfavored in this analysis and are $\sim 50\%$ as likely as the SZ to be the source of the excess. Although the detection of excess power in

TABLE 3
JOINT LIKELIHOOD BAND-POWERS

ℓ range	ℓ_{eff}	q (μK^2)	σ (μK^2)	x (μK^2)
350-550	470	2311	95	-355
550-650	608	2035	94	-311
650-730	695	1930	92	-274
730-790	763	2239	114	-245
790-850	823	2456	118	-262
850-910	884	1873	92	-168
910-970	943	1466	72	-107
970-1030	1003	1141	58	-18
1030-1090	1062	1071	56	17
1090-1150	1122	1174	59	35
1150-1210	1183	1096	56	77
1210-1270	1243	830	47	123
1270-1330	1301	712	44	159
1330-1390	1361	799	48	198
1390-1450	1421	766	47	224
1450-1510	1482	620	45	248
1510-1570	1541	531	42	235
1570-1650	1618	447	35	268
1650-1750	1713	373	31	248
1750-1850	1814	353	33	271
1850-1950	1898	233	34	175
1950-2100	2020	223	32	209
2100-2300	2194	166	32	250
2300-2500	2391	163	44	367
2500-3000	2646	108	46	575

Note. — Band multipole range and weighted value ℓ_{eff} , decorrelated band-powers q_B , uncertainty σ_B , and log-normal offset x_B from the joint likelihood analysis of the 10 ACBAR fields. The PMN radio point source and IRAS dust foreground templates have been projected out in this analysis.

the ACBAR spectrum is more robust than in K07, the constraints on the frequency dependence of the excess are largely unchanged. Additional information on radio and IR sources is needed to eliminate the possibility of multiple foreground contributions.

Alternatively, we can infer the foreground amplitudes which would be required to explain the observed excess in the ACBAR band-powers and compare the inferred amplitudes to those predicted in § 6.2. We subtract the predicted band-powers at $\ell > 1950$ from the measured band-powers in Table 3 and fit the residuals to the functional form of eq. 3. We find a best-fit excess of $q_{src} = 46 \pm 26$. In principle, this excess could be explained by dusty galaxies or radio sources. The major uncertainty in estimating the band-power contribution from dusty galaxies lies in the extrapolating the observations at higher frequencies to 150 GHz. The spectral dependence can be parametrized as $S_\nu \propto \nu^\beta$. We average the β values estimated using number counts from the SHADES survey (Coppin et al. 2006) and the Bolocam Lockman Hole Survey (Maloney et al. 2005). The fluxes of dusty galaxies would need to scale as $S_\nu \propto \nu^{2.03}$ in order to produce an excess of $46 (\ell/2600)^2 \mu K^2$. This would be a nearly black-body spectrum, which is highly unlikely for dust emission. Estimates of β in the literature range from a very conservative 2.6 to 4. As with dusty galaxies, the radio source band-power estimate is sensitive to the assumed spectral

dependence of the sources used to extrapolate the flux cut-off from 4.85 GHz to 150 GHz. Once again expressing it as $S_\nu \propto \nu^{-\beta}$, we find that $\beta = 0.07$ is required to produce the best-fit excess power. This is dramatically higher than the $\beta = -0.67$ estimated from binned source amplitudes in § 6.2.

8. COSMOLOGICAL PARAMETERS

8.1. Cosmological Parameters and their “Prior” Measures

In this section, we estimate cosmological parameters for a minimal inflation-based, spatially-flat, tilted, gravitationally lensed, Λ CDM model characterized by six parameters, and then investigate models with additional parameters to test extensions of the theory. For our base model, the six parameters are: the physical density of baryonic and dark matter, $\Omega_b h^2$ and $\Omega_c h^2$; a uniform spectral index n_s and amplitude $\ln A_s$ of the primordial power spectrum, the optical depth to last scattering, τ ; and θ , the ratio of the sound horizon at last scattering to the angular diameter distance. The primordial comoving scalar curvature power spectrum is expressed as $\mathcal{P}_s(k) = A_s (k/k_*)^{(n_s-1)}$, where the normalization (pivot-point) wavenumber is chosen to be $k_* = 0.05 \text{ Mpc}^{-1}$. The parameter θ maps angles observed at our location to comoving spatial scales at recombination; changing θ shifts the entire acoustic

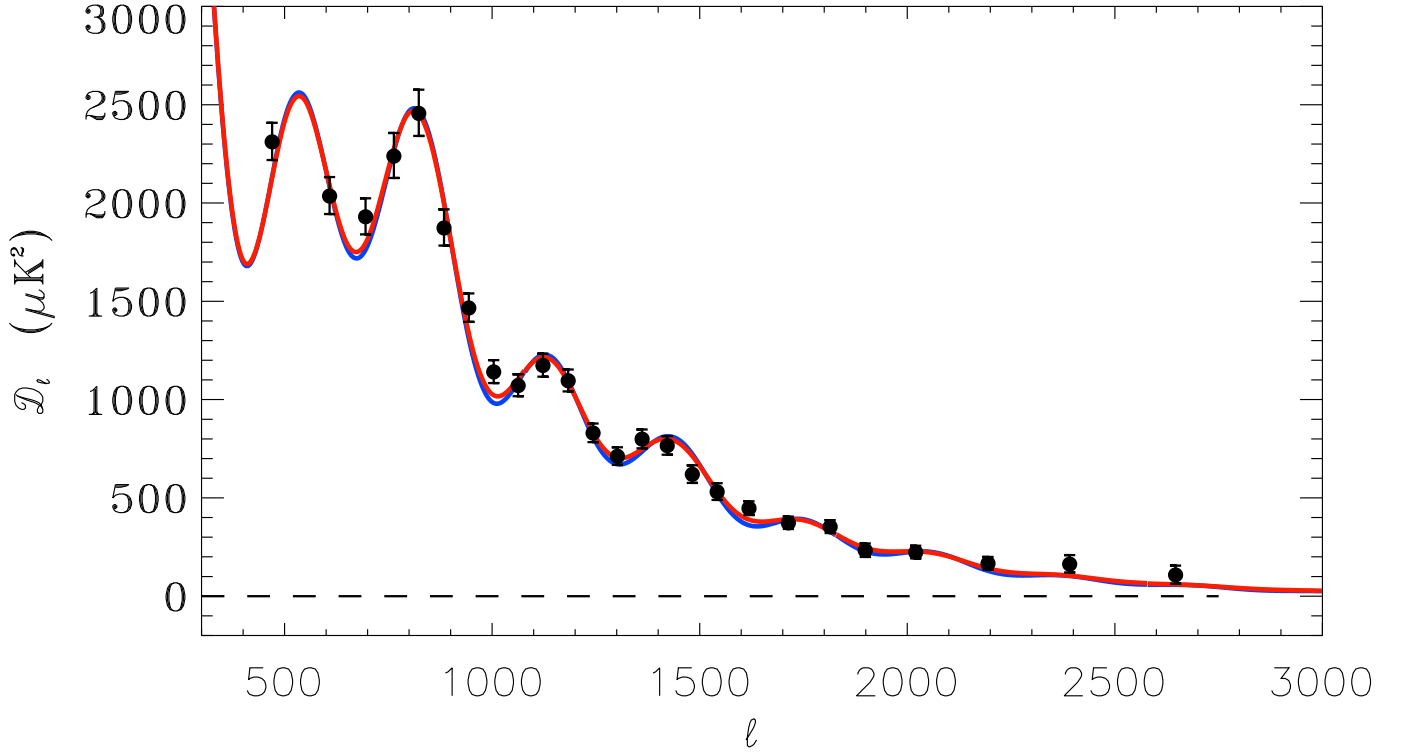


FIG. 5.— The decorrelated ACBAR band-powers for the full data set. The 1σ error bars are derived from the offset-lognormal fits to the likelihood function. The band-powers are in excellent agreement with a Λ CDM model. The damping of the anisotropies is clearly seen with a $S/N > 4$ out to $\ell = 2500$. The third acoustic peak (at $\ell \sim 800$), fourth acoustic peak (at $\ell \sim 1100$), and fifth acoustic peak (at $\ell \sim 1400$) are visible. The plotted lines are the best fits to the ACBAR and WMAP3 band-powers for a spatially flat, Λ CDM universe with no SZ contribution. A lensed (red) and unlensed (blue) model spectrum is shown; the lensed spectrum is a significantly better fit to the ACBAR data.

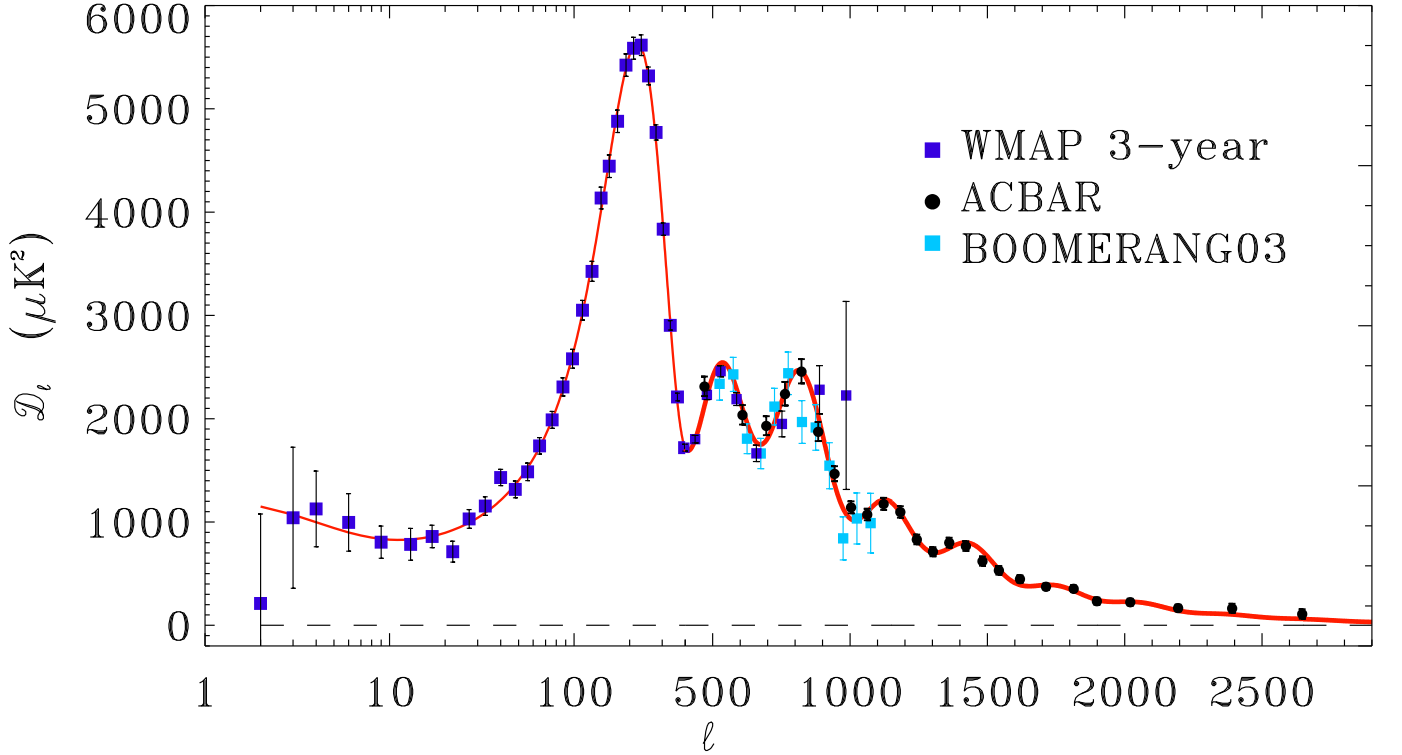


FIG. 6.— The ACBAR band-powers plotted with those from WMAP3 (Hinshaw et al. 2006) and the 2003 flight of BOOMERANG (Jones et al. 2006). The three experiments show excellent agreement in the overlapped region.

peak/valley and damping pattern of the CMB power spec-

tra. Additional parameters are derived from this basic set. These include: the energy density of a cosmological

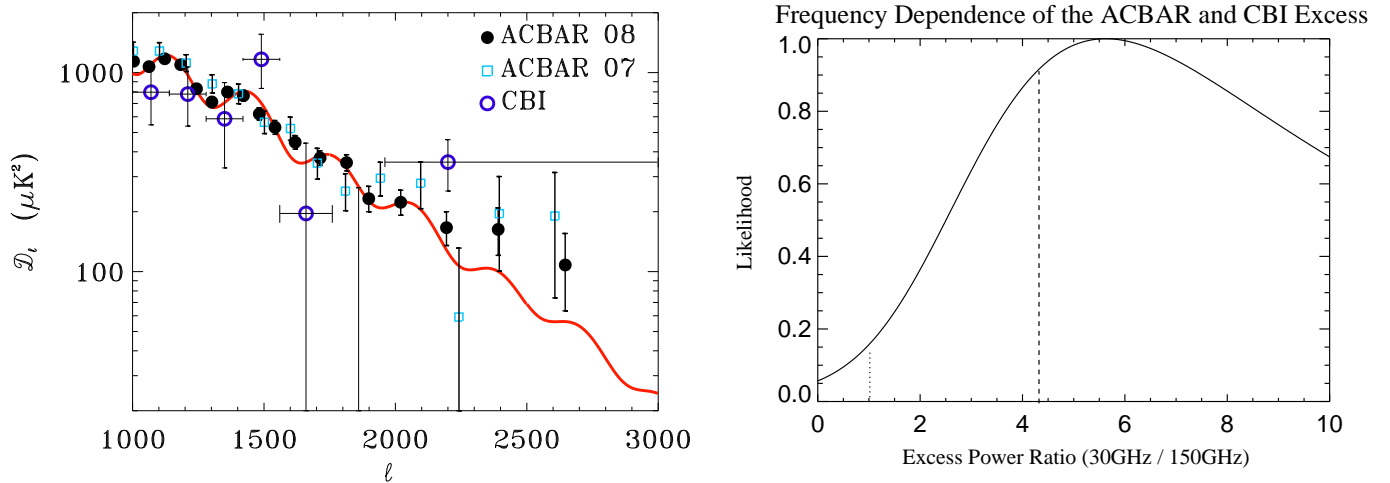


FIG. 7.— ACBAR results on the high- ℓ anisotropies. *Left:* The ACBAR band-powers above $\ell = 1000$ plotted against the best-fit ACBAR+WMAP3 model spectrum. The latest CBI results at 30 GHz and the previous ACBAR results are also shown. The ACBAR band-powers for $\ell > 1950$ are consistently above the model spectrum and below the CBI band-power. *Right:* The likelihood distribution for the ratio of the “excess” power, observed by CBI at 30 GHz and ACBAR at 150 GHz. The excess for each experiment is defined by a flat spectrum for $\ell > 1950$. The likelihood is estimated by examining the difference of the measured band-powers and the model band-powers. The vertical dashed line represents the expected ratio (4.3) for the excess being due to the SZ effect. If the excess power seen in CBI is caused by non-standard primordial processes, the ratio will be unity (blackbody), indicated by the dotted line. If the excess in ACBAR and CBI has a common origin, we conclude that it is 6 times more likely that the excess seen by CBI and ACBAR is caused by the thermal SZ effect than a primordial source.

constant in units of the critical density, Ω_Λ ; the age of the universe; the energy density of non-relativistic matter, Ω_m ; the *rms* (linear) matter fluctuation level in $8h^{-1}\text{Mpc}$ spheres, σ_8 ; the redshift to reionization, z_{re} ; and the value of the present day Hubble constant, H_0 , in units of $\text{km s}^{-1}\text{Mpc}^{-1}$.

Single-field models of inflation predict the existence of a gravitational wave background characterized by a primordial power law $\mathcal{P}_t \sim k^{n_t}$. We characterize the strength by the tensor-to-scalar ratio $r = \mathcal{P}_t/\mathcal{P}_s$ evaluated at a pivot point 0.002Mpc^{-1} . We relate the tilt to r using the approximate consistency relation $n_t \approx -r/8/(1-r/16)$. (We find little difference in the parameters if we just fix n_t to be zero, as has often been assumed when r is included, but using this relation is superior since it is motivated by inflation physics.)

A small running of the spectral index is also expected in slow-roll inflation and we test for this by extending the basic ΛCDM power law model to include a scale dependence of the scalar spectral tilt, $dn_s/d\ln(k)$.

We have also added non-zero curvature Ω_k to our basic six parameters. The results are consistent with the flat case, but with the standard geometrical degeneracy relating Ω_k and Ω_Λ expressed through θ leading to a near-degenerate tail to $\Omega_k < 0$.

The ACBAR spectrum includes band-powers at $\ell > 2000$ where the signal due to secondary CMB anisotropies associated with post-recombination nonlinear effects should become significant. In particular, the thermal Sunyaev-Zel’dovich effect and the contribution of unresolved radio sources and dusty galaxies will ultimately dominate over the primary anisotropy’s damping tail, the only question is at what multipole crossover occurs. Without including such secondary effects, the parameters we derive from the primary anisotropy power spectrum could

be biased. To account for this, we have added to the primary anisotropy power spectrum (1) the SZ template power spectrum $\hat{\mathcal{D}}_\ell^{\text{SZ}}$ used in K07 and (Bond et al. 2005; Goldstein et al. 2003) which was derived from cosmological hydrodynamics simulations and (2) an unclustered point source template, as in eq. 3. Each template is scaled by an overall amplitude parameter, q_{SZ} and q_{src} , which we assume have uniform prior measures with a range much larger than required by the ACBAR data. The white-noise form for $\mathcal{D}_\ell^{\text{src}}$ given by eq. 3, is appropriate for the statistically-averaged power of a distribution of unclustered sources. The clustering of radio sources is not a large effect, but we do expect sub-mm sources associated with dusty galaxies at lower flux levels to be clustered. As mentioned in § 6.2, in spite of great strides in sub-mm observations in recent years, significant uncertainties remain in source fluxes and clustering at 150 GHz. Theoretical models suggest both will be important for a complete treatment, but the approximation adopted here should be sufficient for the ACBAR data set. In the parameter tables below, we show results including these secondary templates. We find the basic parameter central values and uncertainties change little whether we marginalize over either of the two template amplitudes or set them both to zero.

The parameter constraints are obtained using a Monte Carlo Markov Chain (MCMC) sampling of the multi-dimensional likelihood as a function of model parameters. The pipeline is based on the publicly available CosmoMC¹⁵ package (Lewis & Bridle 2002). CMB angular power spectra and matter power spectra are computed using the CAMB code (Lewis et al. 2000). As described in Section 7, we approximate the full non-Gaussian band-power likelihoods with an offset lognormal distribution (Bond et al. 2000). Our standard CosmoMC results

¹⁵ <http://cosmologist.info/cosmomc>

include the effects of weak gravitational lensing on the CMB (Seljak 1996; Lewis et al. 2000). Lensing effects in the temperature spectrum are expected to become significant at scales $\ell > 1000$, hence it is important to include this effect when interpreting the ACBAR results. The major effect of lensing is a scale-dependent smoothing of the angular power spectrum which diminishes the peaks and valleys of the spectrum. Inclusion of lensing in the model improves the fit to the data for all experiment combinations.

The typical computation consists of eight separate chains, each having different initial, random parameter choices. The chains are run until the largest eigenvalue of the Gelman-Rubin test is smaller than 0.01 after accounting for burn-in. Uniform priors with very broad distributions are assumed for the basic parameters. The standard run also includes a weak prior on the Hubble constant ($45 < H_0 < 90 \text{ km s}^{-1} \text{ Mpc}^{-1}$) and on the age of the universe ($> 10 \text{ Gyrs}$), but these have negligible effects. We also investigate the influence of adding Large Scale Structure (LSS) data from the 2 degree Field Galaxy Redshift Survey (2dFGRS) (Cole et al. 2005) and the Sloan Digital Sky Survey (SDSS) (Tegmark et al. 2004). When including the LSS data, we use only the band-powers for length scales larger than $k \sim 0.1 h \text{ Mpc}^{-1}$ to avoid non-linear clustering and scale-dependent galaxy biasing effects. We marginalize over a parameter b_g^2 which describes the (linear) biasing of the galaxy-galaxy power spectrum for L_* galaxies relative to the underlying mass density power spectrum. We adopt a Gaussian prior on b_g^2 centered around $b_g = 1.0$ with a conservative width equivalent to $\delta b_g = 0.3$; all parameters except σ_8 and τ are insensitive to this width.

8.2. Base Parameter Results

The results for the basic spatially flat tilted Λ CDM parameters are presented in Table 4. The confidence limits are obtained by marginalizing the multi-dimensional likelihoods down to one dimension. The median value is obtained by finding the 50% integral of the resulting likelihood function while the lower and upper error limits are obtained by finding the 16% and 84% integrals, respectively. The CMBall data combination includes the ACBAR results presented here and other CMB data sets with published band-powers and window functions: the WMAP 3 year TT, TE, and EE spectra, with the EE not included at higher ℓ as in Hinshaw et al. (2006); the CBI extended mosaic results (Readhead et al. 2004a) and polarization results (Readhead et al. 2004b; Sievers et al. 2005), combined in the manner described in Sievers et al. (2005);¹⁶ the DASI two year results (Halverson et al. 2002); the DASI EE and TE band-powers (Leitch et al. 2005); the VSA final results (Dickinson et al. 2004); the MAXIMA 1998 flight results (Hanany et al. 2000); and the TT, TE, and EE results from the BOOMERANG 2003 flight (Jones et al. 2006; Piacentini et al. 2006; Montroy et al. 2006). Only $\ell > 350$ band-powers are included for BOOMERANG because of overlap with WMAP3 (although inclusion of the lower ℓ results leaves the parameter results essentially unchanged).

While ACBAR and BOOMERANG are both calibrated through WMAP, this is a small contribution to the total uncertainty in the ACBAR calibration and we treat the calibration uncertainties as independent in our parameter analysis. Although the DASI, CBI, and BOOMERANG 2003 EE and TE results for high- ℓ polarization are included, they have little impact on the values of the parameters we obtain.

In all parameter runs, we have used the latest WMAP3 likelihood code (<http://lambda.gsfc.nasa.gov/>) which includes an updated point-source correction, stimulated by (Huffenberger et al. 2006), and foreground marginalization on large angular scales. These updates result in small increases in n_s , Ω_m , and σ_8 compared to those reported in Spergel et al. (2006).

The results for the basic model parameter set with various combinations of data are summarized in Fig. 8 and Table 4. The addition of the ACBAR data to WMAP3 results in close to 1- σ shifts in θ , $\Omega_c h^2$ and σ_8 . The changes are more significant than those found by K07 because of the significant improvement in the ACBAR power spectrum error bars and calibration uncertainty. The shifts to higher values in these parameters remain when the CMBall combination is used. The CMBall combination without ACBAR yields values slightly higher than with WMAP3 only, but not as high as when ACBAR is included ($\theta = 1.042^{+0.003}_{-0.003}$, $\Omega_c h^2 = 0.109^{+0.007}_{-0.007}$, and $\sigma_8 = 0.78^{+0.04}_{-0.04}$).

To explore the tension between the results from WMAP3 and the other (higher resolution) CMB experiments, we tested the sensitivity of the parameter fits to omitting the WMAP3 TT power spectrum points for the third acoustic peak ($\ell > 650$). This is approximately the multipole corresponding to the Gaussian beam width $\ell_s = \sqrt{8 \ln 2} / \theta_{fwhm}$ for the 94 GHz WMAP channel, with the lower WMAP frequencies having correspondingly larger beams and lower ℓ_s . Excluding $\ell > 650$ from the WMAP3 data results in higher values of θ , $\Omega_c h^2$, and σ_8 , which are more compatible with the ACBAR and CMBall results. These results are shown in the second column of Table 4. We conclude that the lower parameter values favored by WMAP3 alone are driven by the points associated with the third peak. We cannot answer whether continued uncertainty in residual point source contributions (Huffenberger et al. 2007; Huffenberger et al. 2006) is a contributing factor, but we do find that the results for the WMAP3+ACBAR and CMBall combinations depend only weakly on the WMAP3 ℓ -cut (e.g. $\sigma_8 = 0.83^{+0.04}_{-0.04}$ and $\theta = 1.045^{+0.003}_{-0.003}$ with and $\sigma_8 = 0.81^{+0.03}_{-0.03}$ and $\theta = 1.044^{+0.003}_{-0.003}$ without the $\ell < 650$ cut for CMBall). Figure 9 summarizes the effects in the θ vs. Ω_m plane of the cuts and data combinations.

The addition of LSS data has little impact on the parameter values, apart from $\Omega_c h^2$ being further increased to $\Omega_c h^2 = 0.116^{+0.005}_{-0.005}$. We have also found that the results do not change significantly from CMBall+LSS when SN1a data are included (in this case from the Riess et al. (2004) gold set), so we have not included a separate column. The SN1a data would be crucial if we were testing the equation of state of dark energy.

All parameter results listed in Tables 4 and 5 include the

¹⁶ We exclude the band powers below $\ell = 600$ from the CBI extended mosaic results to reduce the correlation with the TT band powers of the CBI polarization dataset which influence the sample-dominated end of the spectrum.

effects of weak lensing of the CMB on the resulting power spectrum. For every case including CMB lensing, we have performed an identical calculation neglecting the effects of lensing. Including lensing improves the fit of the model to the observed bandpowers compared to the no-lens runs for all data combinations. This can be quantified by the log-likelihood differences between the lensed and non-lensed best-fit models: for WMAP3 alone it is $\Delta \ln L = 0.84$, increasing to 4.73 with ACBAR included, corresponding to a 3.1σ detection of lensing. The significance of the detection is comparable to the recent WMAP3/NVSS/SDSS cross-correlation results by Smith et al. (2007) and Hirata et al. (2008). The value of $\Delta \ln L$ further increases to 5.42 with CMBall, and 5.69 for the CMBall+LSS data combination. Overall, there are only small shifts in the median value of the parameters when lensing is included, however the most pronounced shifts are in some of the parameters of interest to the discussion above. For the ACBAR+WMAP3 data combination, we find $\sigma_8 = 0.79^{+0.04}_{-0.04} \rightarrow 0.81^{+0.04}_{-0.04}$ and $\Omega_c h^2 = 0.109^{+0.07}_{-0.06} \rightarrow 0.112^{+0.07}_{-0.07}$ when going from non-lensed to lensed models respectively.

We have also run a limited set of non-flat model chains. The models in this case do not include the effect of weak lensing and we keep the same weak prior on H_0 . When $\Omega_k = 0$ is not enforced, the weak prior on H_0 has a significant effect on the result as it restricts the extent of the geometrical degeneracy which is present in this case. For WMAP3 only we obtain $\Omega_k = -0.03^{+0.03}_{-0.09}$ which becomes $\Omega_k = -0.03^{+0.04}_{-0.06}$ when ACBAR is included.

8.3. Residual source marginalization

As discussed in § 8.1, the ACBAR band-powers at $\ell > 1950$ are greater than the predictions of the best-fit models for the primary CMB. In § 7.2, it was shown that accounting for the observed excess by unresolved radio sources and dusty galaxies would require a non-standard extrapolation of their expected flux to 150 GHz. Nonetheless, we explore the effect on the basic parameters if we allow q_{src} to become large enough to explain the observed excess. We marginalize over a wide uniform prior in q_{src} from 0 to $4600 \mu K^2$, i.e. roughly 100 times the power required to fit the high- ℓ points. The results for runs including this marginalization are shown in Tables 4 and 5. We find q_{src} values consistent with the estimate in § 7.2. The template amplitude q_{src} is not well constrained by the fit, and the effect of the marginalization on the basic parameters is negligible. The addition of a source template improves the fit to the high- ℓ points and therefore increases, albeit modestly, the best-fit likelihood: for the ACBAR+WMAP3 combination the change in likelihood is $\Delta \ln L = 0.24$.

Contributions from point sources or the SZ effect are nearly degenerate in the high- ℓ ACBAR band-powers. However, the CMBall combination is potentially sensitive to a SZ contribution because of the SZ frequency dependence. The CBI data which also has an excess at high- ℓ has already included substantial modeling and vetoing of radio sources. In the fits in the tables with SZ, we assume that the residual contribution of the unresolved source background to the CBI band-powers is sufficiently low that we do not require a source template for that data, only the SZ template.

8.4. Sunyaev-Zel'dovich template extension

The amplitude of the SZ signal depends strongly on the overall matter fluctuation amplitude, σ_8 . We have modified our parameter fitting pipeline to allow for extra frequency dependent contributions to the CMB power spectrum and have implemented it in a simple analysis using a fixed template $\hat{\mathcal{D}}_\ell^{\text{SZ}}$ for the shape of the thermal SZ power spectrum. The template was obtained from two large, hydrodynamical simulations of a scale-invariant ($n_s = 1$) Λ CDM model with $\Omega_b h = 0.029$ and with $\sigma_8 = 0.9$ and $\sigma_8 = 1.0$. (See Bond et al. (2005) for a detailed description of the simulations.) Recently the WMAP team have used a different SZ template based on analytic estimations of the power spectrum (Spergel et al. 2006). It is characterized by a slower rise in ℓ than the simulation-based template, which cut nearby clusters out of the power spectrum. There has been no fine-tuning of either spectra to agree with all of the X-ray and other cluster data. This may have an effect on shape, especially at high- ℓ .

The SZ contribution, $\mathcal{D}_\ell^{\text{SZ}} = (q_{\text{SZ}}) f_\nu \hat{\mathcal{D}}_\ell^{\text{SZ}}$, added to the base six-parameter model spectrum has a frequency-dependent SZ pre-factor f_ν . Including this SZ template with all model parameters free to vary is complementary to the analysis of § 7.2 which directly compared the residual CBI and ACBAR band-powers at $\ell > 1950$ for the best fit WMAP3+ACBAR model power spectrum. In that more restrictive analysis, the primary power spectrum is fixed and f_ν is allowed to vary as well as a broad-band excess power. We found the excesses of CBI and ACBAR are not compatible with a uniform f_ν , whereas the factor of 4.3 between f_ν at 30 GHz and 150 GHz appropriate for the SZ effect is quite compatible. This is the motivation of the SZ-restricted template described here. In the hydrodynamical simulations used to derive the SZ template, the amplitude was shown to scale as $q_{\text{SZ}} = (\sigma_8/0.9)^7 (\Omega_b h/0.029)^2$. We consider two cases: (1) the scaling parameter q_{SZ} is slaved to $(\sigma_8/0.9)^7 (\Omega_b h/0.029)^2$, which means that it is primarily determined by the primary CMB data; (2) q_{SZ} is allowed to float freely and an independent σ_8^{SZ} is derived, to be compared with the σ_8 that is derived from the basic six parameters. We use a uniform prior in q_{SZ} in this case with limits $0 \leq q_{\text{SZ}} \leq 4.0$.

Regardless of the data combination, we find that including a SZ component in the model has little effect on the values of most basic cosmological parameters (see Table 4), whether q_{SZ} is related to cosmic parameters through $q_{\text{SZ}} = (\sigma_8/0.9)^7 (\Omega_b h/0.029)^2$ or is allowed to float freely. Note that the SZ results break the $A_s e^{-2\tau}$ near-degeneracy (as does weak lensing, though not as strongly).

When we begin with the combination of the ACBAR and WMAP3 data, we find a freely-floating SZ amplitude results in $q_{\text{SZ}} = 0.88^{+0.27}_{-0.87}$, with no effective lower bound. We can use the above relation of $q_{\text{SZ}}(\sigma_8, \Omega_b h)$ to estimate a corresponding $\sigma_8^{(\text{SZ})} = 0.96^{+0.08(0.13)}_{-0.12(0.28)}$, where the in brackets we have indicated the 2σ errors. The value is higher than but marginally compatible, within the uncertainties, to values obtained from the primary CMB fits alone: the ACBAR + WMAP3 fits in Table 4 give $\sigma_8 = 0.81^{+0.04}_{-0.04}$. The confidence limits of the derived $\sigma_8^{(\text{SZ})}$ also depend strongly on the choice of measure which is uniform in the amplitude q_{SZ} . When the contribution is slaved to the

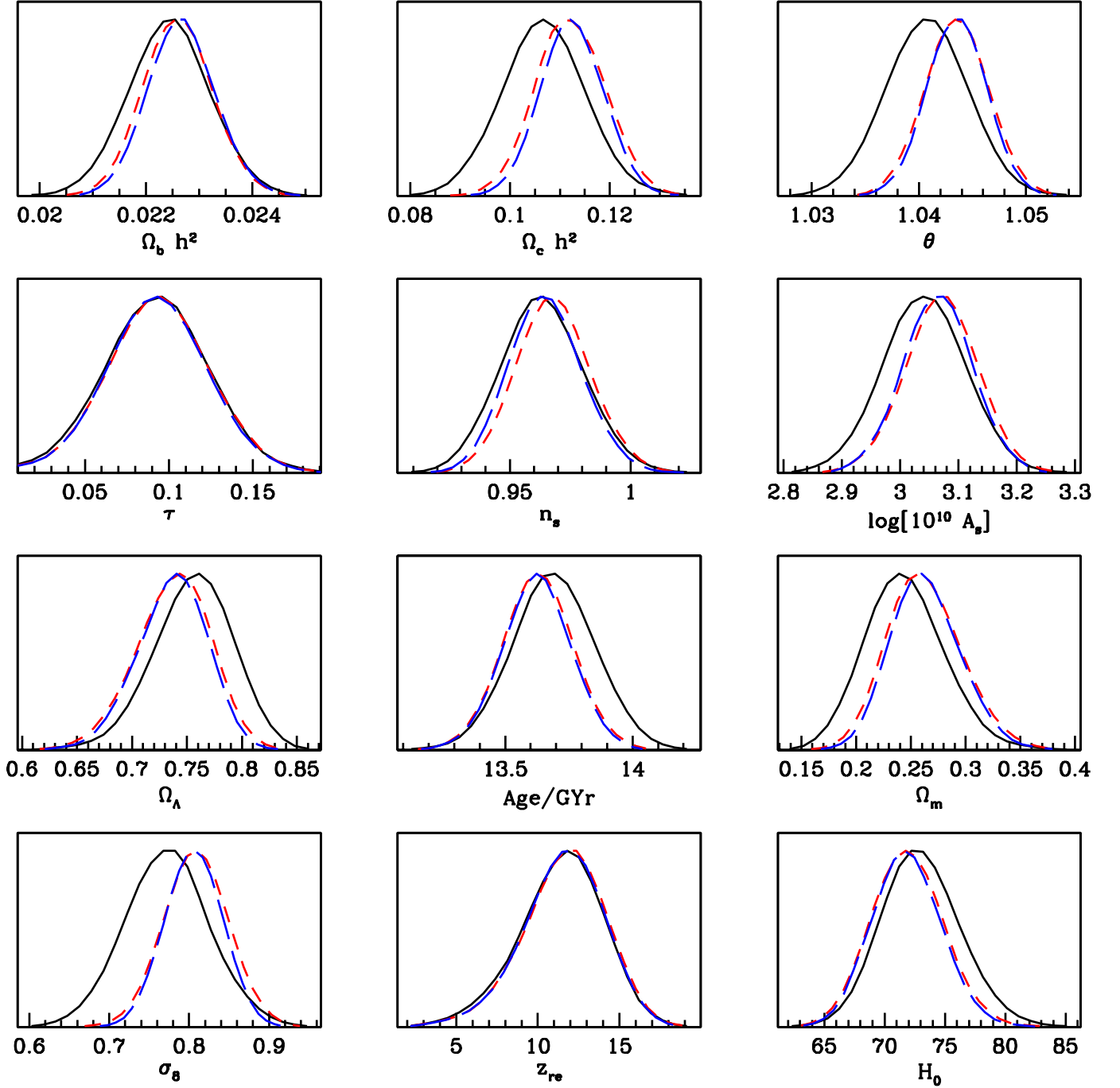


FIG. 8.— Basic parameter marginalized 1-dimensional likelihood distributions for the following data combinations; WMAP3-only (black, solid), ACBAR + WMAP3 (red, short-dashed), CMBall (blue, long-dashed). All runs include lensing.

primary derived σ_8 and $\Omega_b h$ values, there is little effect on the value of σ_8 value itself: we get again $\sigma_8 = 0.81^{+0.04}_{-0.04}$ since the high- ℓ power is not significant enough to draw the value up to the level required to fit the ACBAR band-powers. The effect of slaved and unslaved fits can be seen in Fig. 11.

When the high- ℓ band-powers of CBI and BIMA are included in the analysis, there is a significant detection of excess power. Both the CBI and BIMA band-powers are from 30 GHz interferometric observations and have higher f_ν values than ACBAR. For the slaved case, the errors tighten slightly while the central value remains station-

ary with $\sigma_8 = 0.81^{+0.03}_{-0.03}$. For the floating case, we find $q_{SZ} = 0.78^{+0.07}_{-0.07}$ which maps to $\sigma_8^{(SZ)} = 0.95^{+0.03}_{-0.04}$.

These central values and uncertainties are computed by transforming integrals of the likelihood $L(q_{SZ}, \Omega_b h, \dots)$ over the prior measures to confidence limits for $\sigma_8^{(SZ)}$. Exactly what measure to place on q_{SZ} and therefore on $\sigma_8^{(SZ)}$ is debatable. A measure uniform in $\alpha_{SZ} = q_{SZ}^{1/2}$, as we used in K07 and (Goldstein et al. 2003) translates into a measure $\propto q_{SZ}^{-1/2} dq_{SZ}$ which favors lower values of $\sigma_8^{(SZ)}$ than the measure uniform in q_{SZ} that we have adopted.

TABLE 4
BASIC 6 PARAMETER CONSTRAINTS

	WMAP3	WMAP3 $\mathcal{J}_{\ell < 650}$	WMAP3+ACBAR	CMBall	CMBall+LSS	CMBall+ q_{SZ}	CMBall+SZ+ q_{src}
$\Omega_b h^2$	$0.0224^{+0.0007}_{-0.0007}$	$0.0232^{+0.0009}_{-0.0010}$	$0.0226^{+0.0006}_{-0.0006}$	$0.0227^{+0.0006}_{-0.0006}$	$0.0226^{+0.0006}_{-0.0006}$	$0.0226^{+0.0006}_{-0.0006}$	$0.0226^{+0.0006}_{-0.0006}$
$\Omega_c h^2$	$0.107^{+0.008}_{-0.008}$	$0.118^{+0.015}_{-0.014}$	$0.112^{+0.007}_{-0.007}$	$0.112^{+0.006}_{-0.006}$	$0.116^{+0.005}_{-0.005}$	$0.111^{+0.006}_{-0.006}$	$0.112^{+0.006}_{-0.006}$
θ	$1.041^{+0.004}_{-0.004}$	$1.046^{+0.005}_{-0.005}$	$1.044^{+0.003}_{-0.003}$	$1.044^{+0.003}_{-0.003}$	$1.043^{+0.003}_{-0.003}$	$1.043^{+0.003}_{-0.003}$	$1.043^{+0.003}_{-0.003}$
τ	$0.093^{+0.014}_{-0.014}$	$0.092^{+0.014}_{-0.014}$	$0.094^{+0.013}_{-0.013}$	$0.093^{+0.013}_{-0.013}$	$0.093^{+0.012}_{-0.012}$	$0.091^{+0.013}_{-0.013}$	$0.092^{+0.014}_{-0.013}$
n_s	$0.963^{+0.017}_{-0.016}$	$0.977^{+0.021}_{-0.021}$	$0.968^{+0.015}_{-0.014}$	$0.965^{+0.015}_{-0.014}$	$0.962^{+0.014}_{-0.013}$	$0.961^{+0.014}_{-0.014}$	$0.962^{+0.015}_{-0.014}$
\mathcal{A}_s	$3.04^{+0.07}_{-0.07}$	$3.10^{+0.09}_{-0.09}$	$3.07^{+0.06}_{-0.06}$	$3.06^{+0.06}_{-0.06}$	$3.08^{+0.05}_{-0.06}$	$3.05^{+0.06}_{-0.06}$	$3.06^{+0.06}_{-0.06}$
Ω_Λ	$0.76^{+0.03}_{-0.04}$	$0.72^{+0.05}_{-0.06}$	$0.74^{+0.03}_{-0.03}$	$0.74^{+0.03}_{-0.03}$	$0.72^{+0.02}_{-0.03}$	$0.74^{+0.03}_{-0.03}$	$0.74^{+0.03}_{-0.03}$
Age	$13.7^{+0.2}_{-0.2}$	$13.5^{+0.2}_{-0.2}$	$13.6^{+0.1}_{-0.1}$	$13.6^{+0.1}_{-0.1}$	$13.7^{+0.1}_{-0.1}$	$13.6^{+0.1}_{-0.1}$	$13.6^{+0.1}_{-0.1}$
Ω_m	$0.24^{+0.04}_{-0.03}$	$0.28^{+0.06}_{-0.05}$	$0.26^{+0.03}_{-0.03}$	$0.26^{+0.03}_{-0.03}$	$0.28^{+0.03}_{-0.02}$	$0.26^{+0.03}_{-0.03}$	$0.26^{+0.03}_{-0.03}$
σ_8	$0.77^{+0.05}_{-0.05}$	$0.85^{+0.09}_{-0.09}$	$0.81^{+0.04}_{-0.04}$	$0.81^{+0.03}_{-0.04}$	$0.82^{+0.03}_{-0.03}$	$0.79^{+0.03}_{-0.03}$	$0.80^{+0.03}_{-0.03}$
z_{re}	$11.6^{+2.3}_{-2.7}$	$11.6^{+2.4}_{-2.7}$	$11.8^{+2.3}_{-2.6}$	$11.7^{+2.2}_{-2.5}$	$11.7^{+2.1}_{-2.4}$	$11.5^{+2.2}_{-2.5}$	$11.6^{+2.2}_{-2.5}$
H_0	$72.9^{+3.3}_{-3.0}$	$70.7^{+3.9}_{-3.6}$	$71.9^{+2.9}_{-2.8}$	$71.8^{+2.8}_{-2.7}$	$70.4^{+2.2}_{-2.1}$	$72.3^{+2.7}_{-2.7}$	$71.7^{+2.6}_{-2.6}$
q_{SZ}	-	-	-	-	-	$0.78^{+0.07}_{-0.07}$	-
q_{src}	-	-	-	-	-	-	35^{+13}_{-35}
σ_8^{SZ}	-	-	-	-	-	$0.95^{+0.03}_{-0.04}$	-

Note. — Results for the basic parameter set. The runs all assume flat cosmologies, uniform and broad priors on each of the basic six parameters, and a weak prior on the Hubble constant ($45 < H_0 < 90 \text{ km s}^{-1} \text{ Mpc}^{-1}$) and the age ($> 10 \text{ Gyr}$). Here $\mathcal{A}_s \equiv \log[10^{10} A_s]$. All runs include the effect of weak gravitational lensing on the CMB. Column 6 presents the results when a SZ template characterized by the overall SZ-template-power q_{SZ} is included. To obtain the basic cosmological parameters, q_{SZ} is marginalized. The values of $\sigma_8^{SZ} = q_{SZ}^{1/7} (\Omega_b h)^{2/7}$ are higher than the σ_8 derived from the primary anisotropies. Column 7 shows the results when the point source contribution scaled by q_{src} is included in combination with the SZ-template with q_{SZ} set to $\sigma_8^7 (\Omega_b h)^2$. The marginalization over the extra high- ℓ contributions shows the basic parameter determinations are stable regardless of the high- ℓ excess.

As the cosmological parameters vary, the SZ template may depend on σ_8 and $\Omega_b h$, and certainly depends on the spectral index n_s and astrophysical issues such as the history of energy injection into the cluster system. In a more complete treatment than that presented here, the shape should be modified along with the base cosmological parameters in the MCMC runs.

We caution that the derived $\sigma_8^{(SZ)}$ depends on the SZ template shape, its extension into the higher ℓ regime probed by BIMA, and the prior measure placed upon q_{SZ} .¹⁷ The decrease in log likelihood for the fit to the model when the SZ is taken into account, is $\Delta \ln L = 0.61$ for the ACBAR+WMAP3 combination and increases to $\Delta \ln L = 1.63$ for CMBall+BIMA.

Regardless of the assumed prior, the CMBall+BIMA combination results in a non-zero $\sigma_8^{(SZ)}$; this is supported by the ACBAR data in the absence of an enhanced sub-mm source contribution. Uncertainties for $\sigma_8^{(SZ)}$ are about a factor of two larger than for the σ_8 determined from the primary CMB data and there is a tension at about the 2-sigma level between the two median values. A visual summary of the results is shown in Fig. 12 where we plot both σ_8 and $\sigma_8^{(SZ)}$ against the spectral index for a number of data combinations. The addition of LSS data does not significantly change these results. When the point source or SZ template marginalization is included, σ_8 decreases slightly for the CMBall dataset.

Recent weak lensing results are in basic agreement with the primary σ_8 values when $\Omega_m = 0.26 \pm 0.03$ from Table 4 is used. With 100 deg^2 of lensing data from the combination of the CFHT weak lensing legacy, RCS, Virgos-Descart and GaBaDos surveys, Benjamin et al. (2007) get $\sigma_8 (\Omega_m/0.26)^{0.59} = 0.80 \pm 0.05$. From the CFHT weak lensing legacy survey alone, Fu et al. (2007) get $\sigma_8 (\Omega_m/0.26)^{0.64} = 0.753 \pm 0.043$, and get $\sigma_8 (\Omega_m/0.26)^{0.53} = 0.82 \pm 0.084$ if only large-scale linear-regime results are used. These weak lensing numbers are lower than past published results because of improved treatments of the redshift distribution of the lensed sources.

As shown in Fig. 11, the ACBAR excess could be due to the combination of an enhanced point source contribution with an SZ template at the level predicted from the primary anisotropy σ_8 value, but this is not the case for CMBall and the CBI excess. The SZ analyses with a free-floating amplitude have not included additional foreground sources for CBI, BIMA, or ACBAR. The effect of radio sources extrapolated to 30 GHz has been included in the CBI and BIMA results, and is unlikely to be an important contaminant for ACBAR. Dusty proto-galaxies should not effect CBI and BIMA, but might impact ACBAR. A dual marginalization CMBall+BIMA+ q_{SZ} + q_{src} case would diminish somewhat the supportive role that ACBAR is playing in the SZ interpretation of the CBI+BIMA excess.

¹⁷ We also note that the non-Gaussian nature of the SZ signal was included in the BIMA results but not in the CBI results. The non-Gaussian effect increases the sample variance and tends to open up the allowed range towards lower σ_8 values (Goldstein et al. 2003; Readhead et al. 2004a).

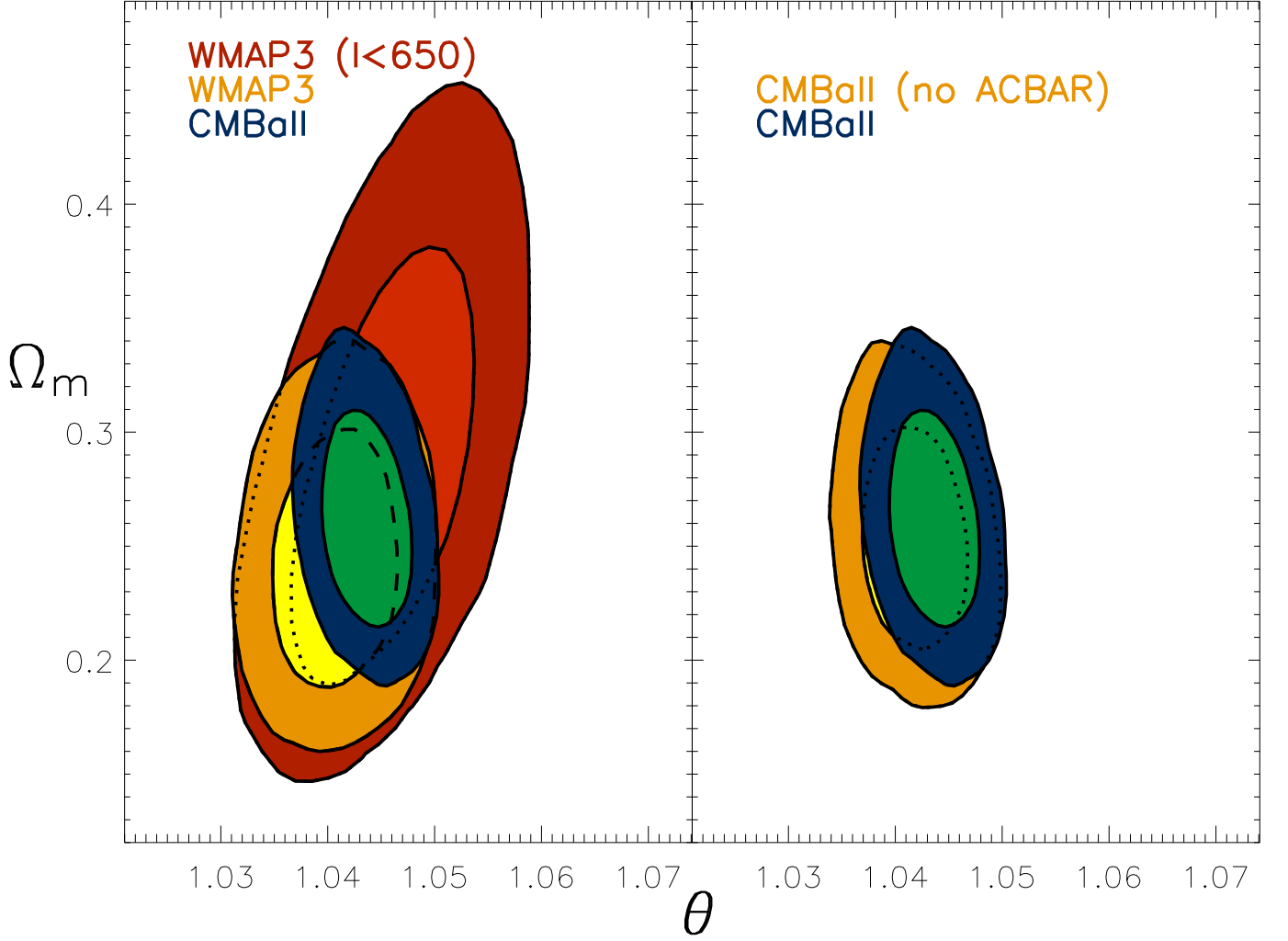


FIG. 9.— 68% and 95% 2D marginalized contours in θ and Ω_m for a number of data combinations. The low solution for θ is preferred by WMAP3 data, but that trend is driven mainly by the power around the third peak as shown by the result when only $\ell < 650$ data is included from WMAP3. When ACBAR is added, the higher values are preferred and the results are similar for the CMBall combination (left panel). The higher θ values are supported by the CMBall combination with or without ACBAR; however, the addition of the ACBAR data leads to an additional increase (right panel).

8.5. Running Spectral Index

There has been interest in the running of the spectral index $dn_s/d\ln k$ since the first release of WMAP data, which showed evidence for a significant negative running when combined with LSS and Lyman alpha forest observations (Spergel et al. 2003). With the precision of the new ACBAR data, we might expect improved constraints on running of the spectral index. To the basic six parameters in the minimal model, we add running of the spectral index $dn_s/d\ln k(k_*)$ around the pivot point $k_* = 0.05 \text{ Mpc}^{-1}$. We adopt the conventionally-used uniform prior in $dn_s/d\ln k(k_*)$, although in usual slow-roll-inflation models, the spectral index fluctuation $\delta n_s \propto \ln(k/k_*) dn_s/d\ln k(k_*)$ is typically restricted by $|1 - n_s|$. Table 5 summarizes the parameter values when running is allowed and demonstrates that its inclusion has only a small effect on the other parameters. For WMAP3 only, we find $dn_s/d\ln k(k_*) = -0.046^{+0.031}_{-0.030}$. The main tendency for the negative value comes from the low- ℓ WMAP3 data. When the ACBAR data is added, the median value shifts closer to zero, $dn_s/d\ln k(k_*) = -0.037^{+0.023}_{-0.023}$, with

a reduced error. The results are nearly identical for the CMBall and CMBall+LSS data combinations. The precise measurement of the high- ℓ CMB power spectrum provided by ACBAR is a potentially powerful constraint on running, but may also include significant contributions from secondary anisotropies and foregrounds. Therefore, in the last two columns we have included the effect of marginalizing over the SZ or point source templates. In both cases, the mean value of the running becomes more negative and more significant. By removing the up-turn associated with the high- ℓ excess, the running can take on the more negative values preferred by WMAP3 alone. A visual representation of the impact of adding the ACBAR data is given in Fig. 10 which shows the correlation between n_s and $dn_s/d\ln k$. The scalar spectral index, $n_s(k_*) = 0.921 \pm 0.032$ for the WMAP3 + ACBAR combination, depends on the choice of pivot point k_* ; a smaller value would yield a higher result while a higher one would give an even lower result.

8.6. Tensor modes

TABLE 5
RUNNING SPECTRAL INDEX PARAMETER CONSTRAINTS

	WMAP3	WMAP3+ACBAR	CMBall	CMBall+LSS	CMBall+ q_{SZ}	CMBall+SZ+ q_{src}
$\Omega_b h^2$	$0.0213^{+0.0010}_{-0.0010}$	$0.0219^{+0.0008}_{-0.0007}$	$0.0220^{+0.0007}_{-0.0007}$	$0.0220^{+0.0006}_{-0.0006}$	$0.0217^{+0.0007}_{-0.0007}$	$0.0217^{+0.0007}_{-0.0007}$
$\Omega_c h^2$	$0.115^{+0.010}_{-0.004}$	$0.121^{+0.009}_{-0.003}$	$0.122^{+0.008}_{-0.008}$	$0.123^{+0.006}_{-0.006}$	$0.123^{+0.008}_{-0.008}$	$0.126^{+0.009}_{-0.003}$
θ	$1.039^{+0.015}_{-0.004}$	$1.043^{+0.015}_{-0.003}$	$1.043^{+0.015}_{-0.003}$	$1.043^{+0.014}_{-0.003}$	$1.043^{+0.015}_{-0.003}$	$1.043^{+0.014}_{-0.003}$
τ	$0.102^{+0.015}_{-0.015}$	$0.105^{+0.015}_{-0.014}$	$0.106^{+0.015}_{-0.014}$	$0.109^{+0.014}_{-0.014}$	$0.106^{+0.015}_{-0.014}$	$0.110^{+0.014}_{-0.014}$
n_s	$0.898^{+0.047}_{-0.046}$	$0.921^{+0.032}_{-0.032}$	$0.919^{+0.030}_{-0.030}$	$0.915^{+0.026}_{-0.025}$	$0.897^{+0.030}_{-0.030}$	$0.898^{+0.031}_{-0.030}$
$dn_s/d\ln(k)$	$-0.046^{+0.031}_{-0.030}$	$-0.037^{+0.023}_{-0.023}$	$-0.037^{+0.022}_{-0.022}$	$-0.041^{+0.019}_{-0.019}$	$-0.051^{+0.021}_{-0.021}$	$-0.052^{+0.023}_{-0.022}$
\mathcal{A}_s	$3.07^{+0.08}_{-0.07}$	$3.12^{+0.07}_{-0.07}$	$3.12^{+0.07}_{-0.07}$	$3.13^{+0.06}_{-0.06}$	$3.11^{+0.07}_{-0.07}$	$3.13^{+0.07}_{-0.06}$
Ω_Λ	$0.71^{+0.05}_{-0.06}$	$0.69^{+0.05}_{-0.06}$	$0.69^{+0.05}_{-0.05}$	$0.68^{+0.03}_{-0.04}$	$0.67^{+0.05}_{-0.05}$	$0.66^{+0.05}_{-0.06}$
Age	$13.9^{+0.2}_{-0.2}$	$13.8^{+0.1}_{-0.2}$	$13.7^{+0.1}_{-0.1}$	$13.8^{+0.1}_{-0.1}$	$13.8^{+0.1}_{-0.1}$	$13.8^{+0.1}_{-0.1}$
Ω_m	$0.29^{+0.06}_{-0.05}$	$0.31^{+0.06}_{-0.05}$	$0.31^{+0.05}_{-0.05}$	$0.32^{+0.04}_{-0.03}$	$0.33^{+0.05}_{-0.05}$	$0.34^{+0.06}_{-0.05}$
σ_8	$0.79^{+0.05}_{-0.05}$	$0.84^{+0.04}_{-0.04}$	$0.84^{+0.04}_{-0.04}$	$0.85^{+0.03}_{-0.03}$	$0.84^{+0.04}_{-0.04}$	$0.85^{+0.04}_{-0.04}$
z_{re}	$13.0^{+2.7}_{-2.9}$	$13.2^{+2.6}_{-2.8}$	$13.3^{+2.6}_{-2.6}$	$13.6^{+2.5}_{-2.6}$	$13.4^{+2.6}_{-2.8}$	$13.9^{+2.5}_{-2.7}$
H_0	$68.4^{+4.3}_{-4.1}$	$67.9^{+3.8}_{-3.6}$	$67.8^{+3.6}_{-3.4}$	$67.3^{+2.6}_{-2.5}$	$66.7^{+3.5}_{-3.3}$	$66.1^{+3.5}_{-3.4}$
q_{SZ}	-	-	-	-	$0.83^{+0.07}_{-0.07}$	-
q_{src}	-	-	-	-	-	37^{+12}_{-37}
σ_8^{qSZ}	-	-	-	-	$0.94^{+0.03}_{-0.04}$	-

Note. — Marginalized parameter constraints for models with a running of the spectral index. The tendency for the low- ℓ data to prefer negative values continues with the higher ℓ data, but at less than 2-sigma for CMB-only. The last two columns include marginalization over extra high- ℓ contributions from SZ and point sources. The basic parameters are stable with respect to the marginalization while the median value for $dn_s/d\ln(k)$ is increased slightly when the SZ or point source contribution is included, although this will be quite sensitive to the details of the template shape.

We have run a limited number of cases including tensor modes, characterizing their strength relative to scalar perturbations by r and fixing the tensor tilt by $n_t \approx -r/8(1-r/16)$. The most stringent upper limit for r is given by the CMBall combination which yields $r < 0.47$ (95% confidence). This assumes a uniform prior measure for r , as is conventional in parameter estimation, although without much justification except that it is conservative. Adding LSS tightens this limit. Our result can be compared with those obtained by Spergel et al. (2006), $r < 0.65$ (95% confidence) for WMAP3 alone and $r < 0.68$ (95% confidence) for WMAP3 + BOOMERANG + ACBAR07.

9. CONCLUSIONS

We have used the complete ACBAR 150 GHz data set to measure the angular power spectrum of the CMB temperature anisotropies. Over three seasons of observation, ACBAR dedicated 85K detector-hours to CMB observations at 150 GHz and covered 1.7% of the sky. The data are calibrated by comparing CMB temperature maps for the largest ACBAR fields with those produced by WMAP3. The new calibration is found to be consistent with the previous planet-based and RCW38-based calibrations, but with the temperature uncertainty reduced to 2.23%.

The ACBAR band-powers reported in Table 3 are the most sensitive measurements to date of CMB temperature anisotropies for multipoles between $\ell \sim 900$ and 3000. The fourth and fifth acoustic peaks are detected for the first time in the ACBAR data. These precise measurements of the CMB temperature anisotropies at high- ℓ are consistent with a spatially flat, dark energy-dominated

Λ CDM cosmology. Including the effects of CMB weak lensing results in a 3.1σ improvement of the model fit to the ACBAR+WMAP3 power spectrum. The excellent fit of the Λ CDM cosmological model to the combined ACBAR+WMAP3 data at $\ell \lesssim 2000$ is a strong confirmation of the standard cosmological paradigm and gives us confidence in the resulting parameter values. The ACBAR data however favors higher median values of σ_8 , Ω_m , and θ than those preferred by WMAP3 alone. This tension appears to be driven by the highest- ℓ WMAP3 results, and is relaxed when including only the $\ell < 650$ TT points. It remains to be seen if this situation will be completely resolved by the impending release of the WMAP 5-year analysis. These higher parameter values remain stable with the inclusion of additional CMB and LSS data, however, the tension is somewhat reduced with the marginalization over an SZ or point source template. After the marginalization, the fits still favor a value of $\sigma_8 \sim 0.80$ which is larger than that preferred by WMAP3 alone.

We have applied strict jackknife tests to the data and find that the results are free of significant systematic errors. We have removed templates derived from the FDS99 dust model and the PMN radio source catalog from the ACBAR maps before estimating the band-powers and find the residual contributions from these foregrounds to be negligible at the current sensitivity. The flux contribution from dusty proto-galaxies is likely to be below the reported band-power uncertainties, but remains poorly constrained due to our incomplete knowledge of the spectral dependence of these sources.

Secondary anisotropies are expected to become important at small angular scales. The ACBAR band-powers

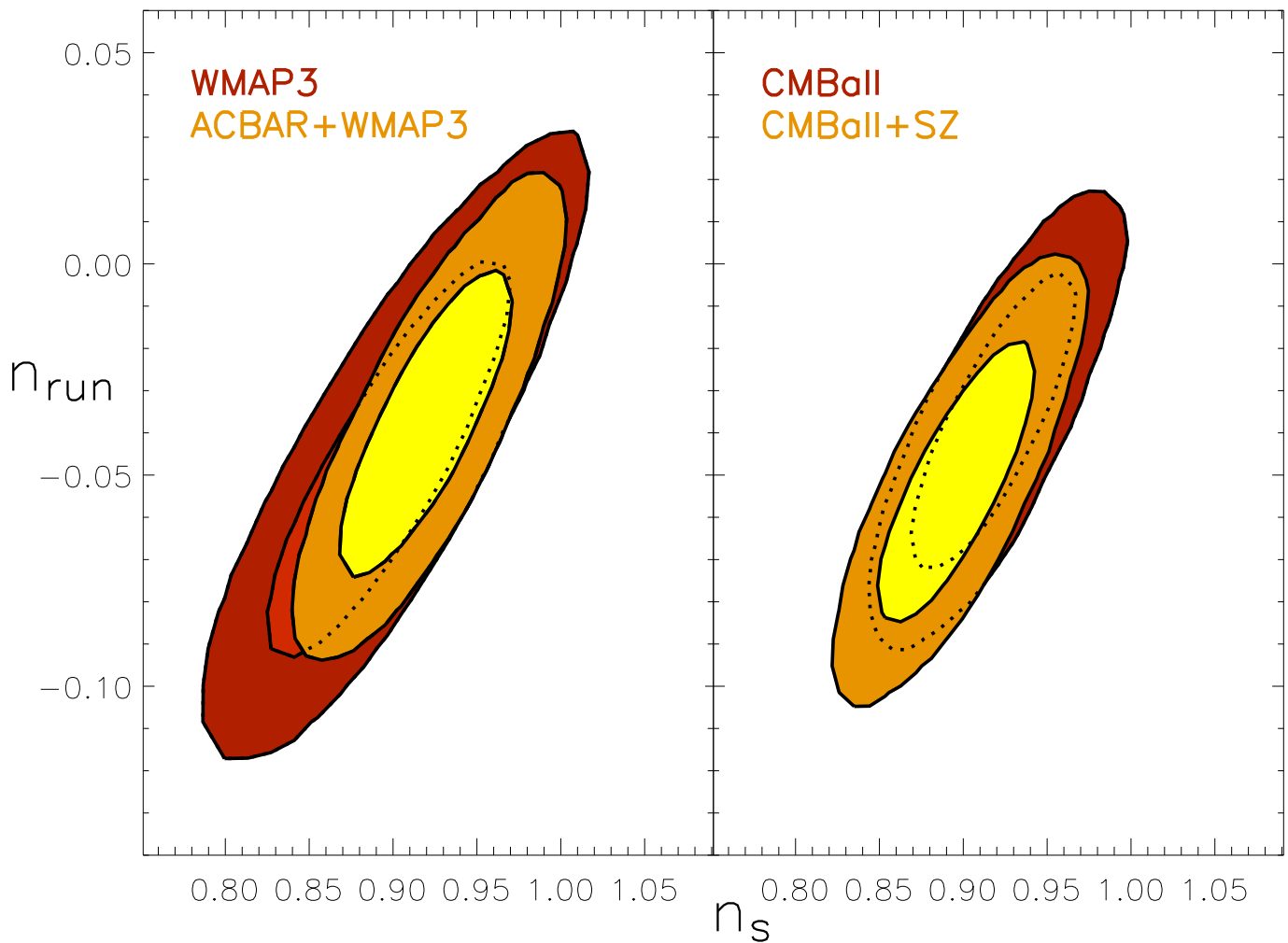


FIG. 10.— 68% and 95% 2D marginalized contours in n_s and $n_{run} = dn_s/d\ln k$. The left panel shows the results for the WMAP3 and ACBAR+WMAP3 combinations. The right panel shows the effect of adding the rest of the CMB data and marginalizing over the SZ template. The basic parameters are quite stable in values and error bars if we marginalize over one or the other of the two template amplitudes, or set them to zero.

are slightly higher (1.7σ) than expected for the primary CMB anisotropies at multipoles above $\ell \sim 2000$. We conduct a joint analysis of the CBI (at 30 GHz) and ACBAR (at 150 GHz) band-powers in the multipole range of $2000 \lesssim \ell \lesssim 3000$. Assuming a common source for the excess in both experiments, the signal has a spectral dependence consistent with the Sunyaev-Zel'dovich effect but not with primary CMB anisotropy. Higher sensitivity observations over a broad range of frequencies will be required to fully characterize CMB secondary anisotropies and eliminate potential foreground contamination.

The ACBAR program has been primarily supported by NSF office of polar programs grants OPP-8920223

and OPP-0091840. This research used resources of the National Energy Research Scientific Computing Center, which is supported by the Office of Science of the U.S. Department of Energy under Contract No. DE-AC03-76SF00098. Chao-Lin Kuo acknowledges support from a NASA postdoctoral fellowship and Marcus Runyan acknowledges support from a Fermi fellowship. Christian Reichardt acknowledges support from a National Science Foundation Graduate Research Fellowship. Some of the results in this paper have been derived using the HEALPix (Górski et al. 2005) package. We thank members of the BOOMERANG team, in particular Brendan Crill, Bill Jones, and Tom Montroy for providing access to the B03 data, the pipeline used to generate simulation maps, and assistance with its operation.

APPENDIX

A. CALIBRATION

The calibration used in K07 was linked to the Boomerang03 (B03) calibration with observations of RCW38. In this section, we describe a new calibration using an a_{lm} -based comparison of CMB structure observed by WMAP3 and ACBAR in 2005. This method is inspired by the calibration scheme used to calibrate B03 to WMAP. The 2005 calibration is carried

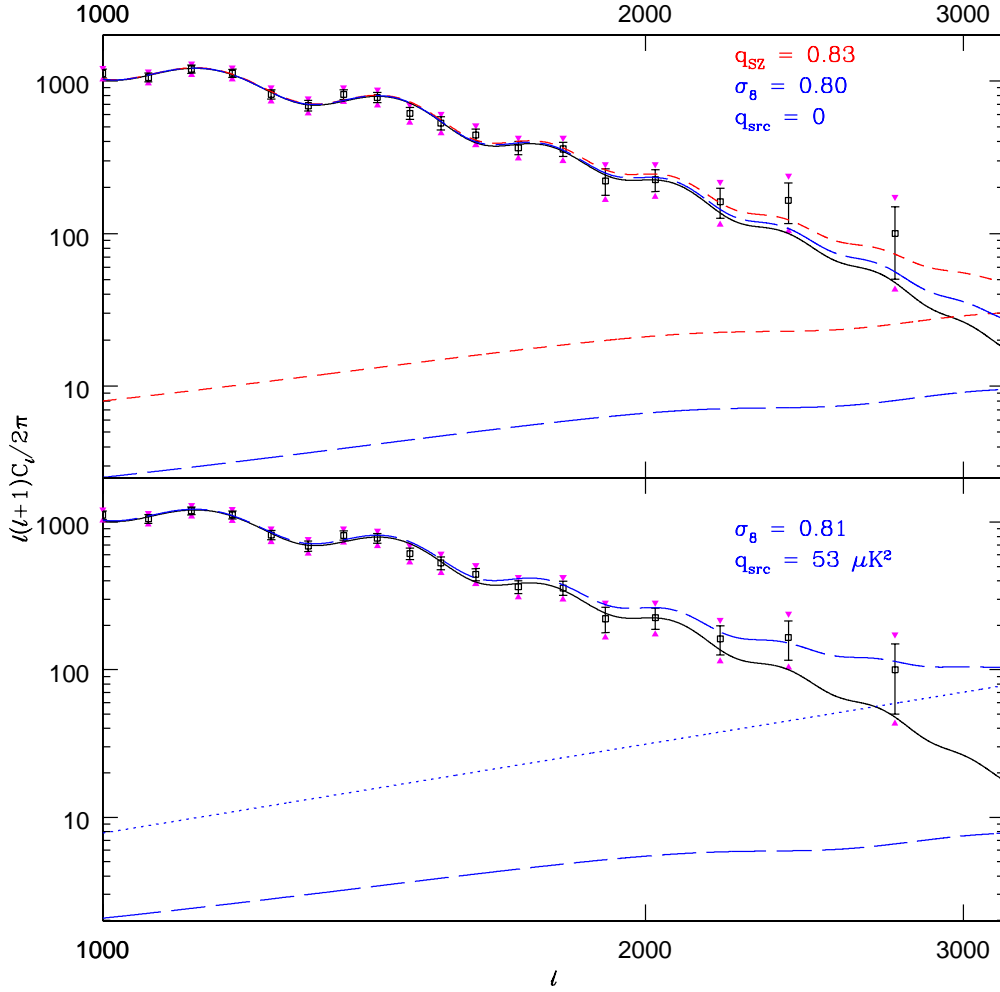


FIG. 11.— Best-fit models for the ACBAR + WMAP3 combination. Only the $\ell > 1000$ ACBAR bandpowers are shown. The arrows are indicative of the possible (coherent) shift in the 1- σ confidence limits due to beam error. The top panel shows fits with just primary CMB (black, solid) and with an extra SZ contribution. The case where the SZ template is scaled independently as q_{SZ} gives the best fit to the high- ℓ excess (red, short-dashed) with $q_{SZ} = 0.83$. The case where the SZ amplitude is slaved to the cosmological parameters $\sigma_8^2(\Omega_b h)^2$ (blue, long-dashed) does not yield enough power to fit the excess given the best-fit value of $\sigma_8 = 0.8$. The bottom panel shows the case when a point source contribution scaled by q_{src} is included for ACBAR together with the slaved SZ contribution (blue, dotted). In this case the best-fit model has $\sigma_8 = 0.81$ determining the sub-dominant SZ contribution and $q_{src} = 53 \mu K^2$ determining the point source contribution.

to other years by an ACBAR-ACBAR power spectrum comparison on fields observed in both years. The WMAP-ACBAR cross-calibration method is described below, with a detailed accounting of uncertainty in Table A6.

WMAP-ACBAR Calibration Calibrating with the CMB temperature anisotropies has two main advantages. The first is that the calibration of the WMAP temperature maps (at 0.5% in temperature) is an order of magnitude more precise than the flux calibration of the calibration sources ACBAR used in previous releases. The second advantage is that the anisotropies have the same spectrum as what is being calibrated, rendering the large frequency gap between WMAP and ACBAR irrelevant.

The two experiments have different scan patterns, noise, beam widths, and spatial filters that will effect the measured flux. In this analysis, we assume that the WMAP3 maps are effectively unfiltered except for the instrumental beam function. The two maps can then be represented as:

$$S_i^{WMAP} = \int T(x) B_{WMAP}(x_i - x) dx + N_i^{WMAP}$$

$$S_i^{ACBAR} = F_{ij} \int T(x) B_{ACBAR}(x_j - x) dx + N_i^{ACBAR}$$

where T is the underlying CMB signal, N is the instrumental noise, B is the beam function, and F_{ij} is the ACBAR filter matrix as defined in Section 3. We reduce the filtering differences by resampling the WMAP map using the ACBAR

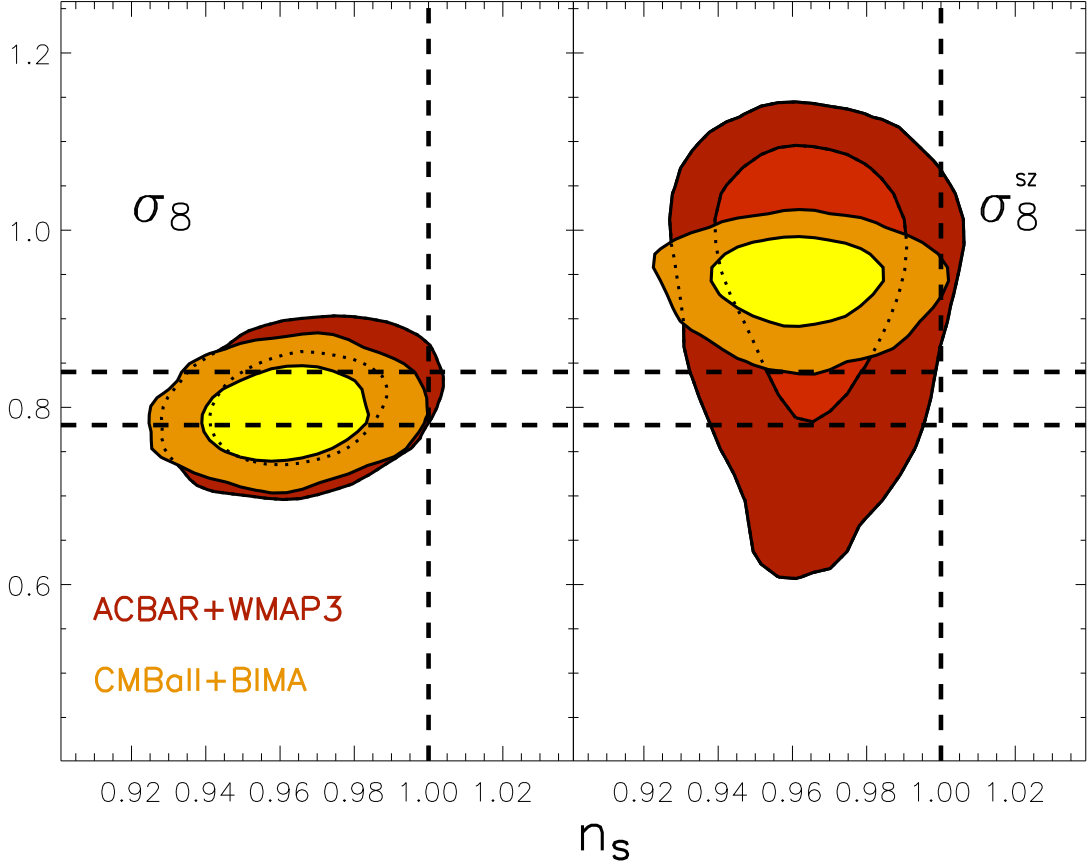


FIG. 12.— The figure contrasts the one and two sigma contour intervals for σ_8 determined from the primary anisotropy component of the CMB (left) with the value inferred from the SZ template transformation of q_{SZ} into $\sigma_8^{(SZ)}$ (right), assuming a uniform prior measure in q_{SZ} . These panels also shows visually the strength of the deviation of n_s from unity for the flat Λ CDM model.

pointing information and applying the ACBAR spatial filtering to generate an ‘ACBAR-filtered’ WMAP map.

$$S_i^{WMAP-equivalent} = F_{ij} \left(\int T(x) B_{WMAP}(x_j - x) dx + N_i^{WMAP} \right)$$

The results of applying this algorithm to the B03 map is shown in Figure A13. We choose to do the absolute calibration via cross-power spectra rather than a direct pixel-to-pixel comparison of the maps. Using cross-spectra significantly reduces the impact of the noise model on the result. The significant beam differences between the experiments are more naturally dealt with in multipole space than in pixel space. We construct the ratio from the filtered maps:

$$R = \Re \left(\left\langle \frac{a_{\ell m}^{WMAP-X} * a_{\ell m}^{ACBAR-Z}}{a_{\ell m}^{ACBAR-Y} * a_{\ell m}^{ACBAR-Z} (B_{\ell}^{WMAP-X} / B_{\ell}^{ACBAR})} \right\rangle \right)$$

where X can denote either the V- or W-band map for WMAP and Y/Z marks either of two noise-independent ACBAR combinations. There is a narrow ℓ -range from 256-512 useful for calibration. The range is limited at high- ℓ by the rapidly falling WMAP beam function and at low- ℓ by the ACBAR polynomial filtering which acts as a high-pass filter. We choose to use the WMAP V & W bands to take advantage of their smaller beam size.

Monte Carlo simulations are used to determine the transfer function of this estimator. We generate CMB sky simulations convolved with the respective instrumental beam functions using the Healpix¹⁸ library. We resample each realization and apply the ACBAR filtering matrix described above to generate equivalent maps for each field. We expected and found a small intrinsic bias as the beam convolution and filtering operations do not commute: $B^{ACBAR} * F_{ij} B^{WMAP} \neq B^{WMAP} * F_{ij} B^{ACBAR}$. We correct the real data by the ℓ -dependent transfer function measured in these simulations. The technique is easily adapted to estimate the error caused by pointing uncertainties and to confirm that the estimator is unbiased with the inclusion of noise. The derived error in the transfer function is listed in Table A6.

Foreground sources have the potential to systematically bias a calibration bridging 60 to 150 GHz. Radio sources, synchrotron emission, dust, and free-free emission all have a distinctly different spectral dependence than the CMB,

¹⁸ <http://healpix.jpl.nasa.gov>

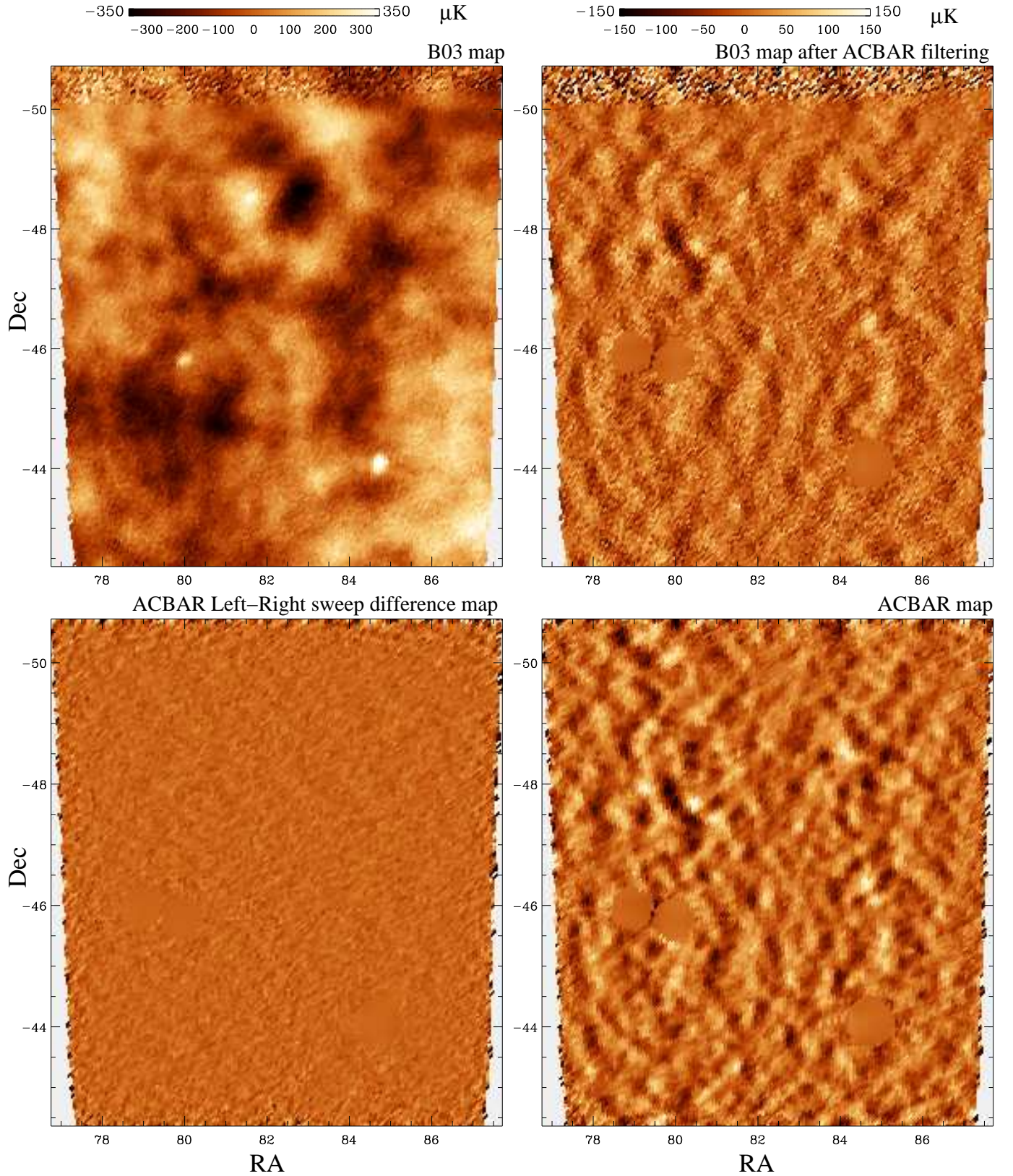


FIG. A13.— A comparison of observations of the CMB8 field made with B03 and ACBAR. This field lies in the deep region of the B03 map. The top two maps are from B03. The bottom two maps are from ACBAR. In the *top left* panel, the B03 map of the CMB8 field. The dynamic range of this map is greater than that of the other three figures. The increased noise at one edge marks the edge of the B03 deep coverage. The ACBAR filtering is applied to the B03 map to create the map in the *top right* panel. Directly below it in the *bottom right* panel is the ACBAR map of same region. Note the clear correspondence between the CMB anisotropies observed by B03 and ACBAR. Three bright point sources have been masked. An ACBAR left-right sweep difference map is shown in the *bottom left* panel. The power spectrum of this map (and the other 9 fields) is plotted in Fig. 3.

TABLE A6
ERROR BUDGET FOR THE $a_{\ell m}$ -BASED ACBAR CALIBRATION

Source	Uncertainty (%)
Statistical Error in the Calibration ratio	1.32
ℓ dependence of the Calibration ratio	1.1
Statistical Error in the Transfer Function of the Calibration ratio	0.35
Uncertainty in the WMAP B_ℓ	0.5
Relative pointing uncertainty	1.0
Uncertainty in the Year-to-year ACBAR calibration	0.3
Uncertainty in the Transfer Function for the Power Spectrum	0.5
Contamination from foregrounds	0.2
WMAP3's Absolute Calibration	0.5
Overall	2.23%

Note. — The calibration of ACBAR using the WMAP3 temperature maps has multiple potential sources of error, tabulated here for reference. The dominant calibration uncertainties are due to noise in the WMAP maps at the angular scales used for calibration. The uncertainty in the ACBAR beam function is comparable to the calibration uncertainty.

which could lead to a calibration bias. This risk is ameliorated by the positioning of the ACBAR fields in regions of exceptionally low foregrounds. Bright radio sources detected in either experiment are masked and excluded from the calibration. The calibration proved insensitive to the exact threshold for source masking. We use the MEM foreground models in Hinshaw et al. (2006) to estimate the RMS fluctuations of each foreground relative to the CMB fluctuations and find that the free-free and synchrotron fluctuations are less than 0.1% of the CMB fluctuations in all frequency bands while dust emission can reach 1.5% of CMB fluctuations in the 150 GHz maps. We test the effects of the most significant foreground, dust, by adding the FDS99 dust model (Finkbeiner et al. 1999) to a set of CMB realizations. The resultant maps are passed through a simulated pipeline as outlined in the previous paragraph. We find that the addition of dust does not introduce a detectable bias with an uncertainty of 0.2%.

We perform a weighted average of the measured calibration ratio across all ℓ -bin, field and band combinations after correcting for the estimated signal-only transfer functions. We estimate the calibration error to be 2.17% for the 2005 data. Table A6 tabulates the contributing factors and error budget. We then propagate this $a_{\ell m}$ -based calibration to the CMB observations done in 2001 and 2002.

ACBAR 2001-2002 and 2002-2005 Cross Calibrations We propagate the 2005 calibration into 2001 and 2002 by comparing the 2001 observations of the CMB2 field to the overlapping 2002 CMB4 field, and the 2002 observations of the CMB5 field to the 2005 observations of the CMB5 field. A power spectrum is calculated for each overlapping region and the ratio of the bandpowers is used to derive a cross calibration. The procedures used are outlined in more detail in K07. We use the same relative calibration for 2001 as K07: $T_{2001}/T_{2002} = 1.238 \pm 0.067$. We find cross-calibration factor for 2002 to be $T_{2005}/T_{2002} = 1.035 \pm 0.025$. We apply these corrections to the data and determine the overall calibration uncertainty to be 2.23% (in temperature units) based primarily on the uncertainties associated with WMAP/ACBAR-2005 cross calibration.

REFERENCES

- Albrecht, A., Coulson, D., Ferreira, P., & Magueijo, J. 1996, *Physical Review Letters*, 76, 1413
- Benjamin, J. et al. 2007, submitted, astro-ph/0703570
- Bond, J. R., Contaldi, C. R., Pen, U.-L., Pogosyan, D., Prunet, S., Ruetalo, M. I., Wadsley, J. W., Zhang, P. and Mason, B. S., Myers, S. T., Pearson, T. J., Readhead, A. C. S., Sievers, J. L., & Udomprasert, P. S. 2005, *ApJ*, 626, 12
- Bond, J. R., Contaldi, C. R., Pen, U.-L., Pogosyan, D., Prunet, S., Ruetalo, M. I., Wadsley, J. W., Zhang, P., Mason, B. S., Myers, S. T., Pearson, T. J., Readhead, A. C. S., Sievers, J. L., & Udomprasert, P. S. 2005, *ApJ*, 626, 12
- Bond, J. R., Jaffe, A. H., & Knox, L. 1998, *Phys. Rev. D*, 57, 2117
- . 2000, *ApJ*, 533, 19, astro-ph/9808264
- Borys, C., Chapman, S., Halpern, M., & Scott, D. 2003, *MNRAS*, 344, 385
- Bridle, S. L., Lewis, A. M., Weller, J., & Efstathiou, G. 2003, *MNRAS*, 342, L72
- Burles, S., Nollett, K. M., & Turner, M. S. 2001, *Phys. Rev. D*, 63, 063512, astro-ph/0008495
- Cole, S., Percival, W. J., Peacock, J. A., Norberg, P., Baugh, C. M., Frenk, C. S., Baldry, I., Bland-Hawthorn, J., Bridges, T., Cannon, R., Colless, M., Collins, C., Couch, W., Cross, N. J. G., Dalton, G., Eke, V. R., De Propris, R., Driver, S. P., Efstathiou, G., Ellis, R. S., Glazebrook, K., Jackson, C., Jenkins, A., Lahav, O., Lewis, I., Lumsden, S., Maddox, S., Madgwick, D., Peterson, B. A., Sutherland, W., & Taylor, K. 2005, *MNRAS*, 362, 505
- Cooray, A., Hu, W., & Tegmark, M. 2000, *ApJ*, 540, 1
- Cooray, A. & Melchiorri, A. 2002, *Phys. Rev. D*, 66, 083001

- Coppin, K., Chapin, E. L., Mortier, A. M. J., Scott, S. E., Borys, C., Dunlop, J. S., Halpern, M., Hughes, D. H., Pope, A., Scott, D., Serjeant, S., Wagg, J., Alexander, D. M., Almaini, O., Aretxaga, I., Babbedge, T., Best, P. N., Blain, A., Chapman, S., Clements, D. L., Crawford, M., Dunne, L., Eales, S. A., Edge, A. C., Farrah, D., Gaztañaga, E., Gear, W. K., Granato, G. L., Greve, T. R., Fox, M., Ivison, R. J., Jarvis, M. J., Jenness, T., Lacey, C., Lepage, K., Mann, R. G., Marsden, G., Martinez-Sansigre, A., Oliver, S., Page, M. J., Peacock, J. A., Pearson, C. P., Percival, W. J., Priddey, R. S., Rawlings, S., Rowan-Robinson, M., Savage, R. S., Seigar, M., Sekiguchi, K., Silva, L., Simpson, C., Smail, I., Stevens, J. A., Takagi, T., Vaccari, M., van Kampen, E., & Willott, C. J. 2006, *MNRAS*, 372, 1621
- Dawson, K. S., Holzzapfel, W. L., Carlstrom, J. E., Joy, M., & LaRoque, S. J. 2006, *ApJ*, 647, 13
- Dickinson, C., Battye, R. A., Carreira, P., Cleary, K., Davies, R. D., Davis, R. J., Genova-Santos, R., Grainge, K., Gutiérrez, C. M., Hafez, Y. A., Hobson, M. P., Jones, M. E., Kneissl, R., Lancaster, K., Lasenby, A., Leahy, J. P., Maisinger, K., Ödman, C., Pooley, G., Rajguru, N., Rebolo, R., Rubiño-Martín, J. A., Saunders, R. D. E., Savage, R. S., Scaife, A., Scott, P. F., Slosar, A., Sosa Molina, P., Taylor, A. C., Titterton, D., Waldram, E., Watson, R. A., & Wilkinson, A. 2004, *MNRAS*, 353, 732
- Finkbeiner, D. P., Davis, M., & Schlegel, D. J. 1999, *ApJ*, 524, 867
- Fu, L. et al. 2007, submitted, arXiv:0712.0884 [astro-ph]
- Goldstein, J. H., Ade, P. A. R., Bock, J. J., Bond, J. R., Cantalupo, C., Contaldi, C. R., Daub, M. D., Holzzapfel, W. L., Kuo, C., Lange, A. E., Lueker, M., Newcomb, M., Peterson, J. B., Pogosyan, D., Ruhl, J. E., Runyan, M. C., & Torbet, E. 2003, *ApJ*, 599, 773
- Górski, K. M., Hivon, E., Banday, A. J., Wandelt, B. D., Hansen, F. K., Reinecke, M., & Bartelmann, M. 2005, *ApJ*, 622, 759
- Greve, T. R., Ivison, R. J., Bertoldi, F., Stevens, J. A., Dunlop, J. S., Lutz, D., & Carilli, C. L. 2004, *MNRAS*, 354, 779
- Griffiths, L. M., Kunz, M., & Silk, J. 2003, *MNRAS*, 339, 680
- Halverson, N. W., Leitch, E. M., Pryke, C., Kovac, J., Carlstrom, J. E., Holzzapfel, W. L., Dragovan, M., Cartwright, J. K., Mason, B. S., Padin, S., Pearson, T. J., Readhead, A. C. S., & Shepherd, M. C. 2002, *ApJ*, 568, 38
- Hanany, S., Ade, P. A., Balbi, A., Bock, J., Borrill, J., Boscaleri, A., de Bernardis, P., Ferreira, P. G., Hristov, V. V., Jaffe, A. H., Lange, A. E., Lee, A. T., Mauskopf, P. D., Netterfield, C. B., Oh, S., Pascale, E., Rabi, B., Richards, P. L., Smoot, G. F., Stompor, R., Winant, C. D., & Wu, J. H. P. 2000, *ApJ*, 545, L5
- Hinshaw, G., Spergel, D. N., Verde, L., Hill, R. S., Meyer, S. S., Barnes, C., Bennett, C. L., Halpern, M., Jarosik, N., Kogut, A., Komatsu, E., Limon, M., Page, L., Tucker, G. S., Weiland, J. L., Wollack, E., & Wright, E. L. 2006, *apj*, submitted, "astro-ph/0603451"
- Hirata, C. M., Ho, S., Padmanabhan, N., Seljak, U., & Bahcall, N. 2008, *ArXiv e-prints*, 801
- Huffenberger, K. M., Eriksen, H. K., & Hansen, F. K. 2006, *ArXiv Astrophysics e-prints*
- Huffenberger, K. M., Eriksen, H. K., Hansen, F. K., Banday, A. J., & Gorski, K. M. 2007, submitted, arXiv:0710.1873 [astro-ph]
- Jones, W. C., Ade, P. A. R., Bock, J. J., Bond, J. R., Borrill, J., Boscaleri, A., Cabella, P., Contaldi, C. R., Crill, B. P., de Bernardis, P., De Gasperis, G., de Oliveira-Costa, A., De Troia, G., di Stefano, G., Hivon, E., Jaffe, A. H., Kisner, T. S., Lange, A. E., MacTavish, C. J., Masi, S., Mauskopf, P. D., Melchiorri, A., Montroy, T. E., Natoli, P., Netterfield, C. B., Pascale, E., Piacentini, F., Pogoyan, D., Polenta, G., Prunet, S., Ricciardi, S., Romeo, G., Ruhl, J. E., Santini, P., Tegmark, M., Veneziani, M., & Vittorio, N. 2006, *ApJ*, 647, 823
- Knox, L. 1999, *Phys. Rev. D*, 60, 103516, astro-ph/9902046
- Knox, L., Holder, G., & Church, S. 2004, *ApJ*, 612, 96
- Komatsu, E. & Seljak, U. 2002, *MNRAS*, 336, 1256
- Kuo, C. L., Ade, P. A. R., Bock, J. J., Bond, J. R., Contaldi, C. R., Daub, M. D., Goldstein, J. H., Holzzapfel, W. L., Lange, A. E., Lueker, M., Newcomb, M., Peterson, J. B., Reichardt, C., Ruhl, J., Runyan, M. C., & Staniszewski, Z. 2007, *ApJ*, 664, 687
- Kuo, C. L., Ade, P. A. R., Bock, J. J., Cantalupo, C., Daub, M. D., Goldstein, J. H., Holzzapfel, W. L., Lange, A. E., Lueker, M., Newcomb, M., Peterson, J. B., Ruhl, J. E., Runyan, M. C., & Torbet, E. 2004, *ApJ*, 600, 32
- Laurent, G. T., Aguirre, J. E., Glenn, J., Ade, P. A. R., Bock, J. J., Edgington, S. F., Goldin, A., Golwala, S. R., Haig, D., Lange, A. E., Maloney, P. R., Mauskopf, P. D., Nguyen, H., Rossinot, P., Sayers, J., & Stover, P. 2005, *ApJ*, 623, 742
- Leach, S. M. & Liddle, A. R. 2003, *MNRAS*, 341, 1151
- Leitch, E. M., Kovac, J. M., Halverson, N. W., Carlstrom, J. E., Pryke, C., & Smith, M. W. E. 2005, *ApJ*, 624, 10
- Lewis, A. & Bridle, S. 2002, *Phys. Rev. D*, 66, 103511
- Lewis, A., Challinor, A., & Lasenby, A. 2000, *ApJ*, 538, 473
- Maloney, P. R., Glenn, J., Aguirre, J. E., Golwala, S. R., Laurent, G. T., Ade, P. A. R., Bock, J. J., Edgington, S. F., Goldin, A., Haig, D., Lange, A. E., Mauskopf, P. D., Nguyen, H., Rossinot, P., Sayers, J., & Stover, P. 2005, *ApJ*, 635, 1044
- Mason, B. S., Pearson, T. J., Readhead, A. C. S., Shepherd, M. C., Sievers, J., Udomprasert, P. S., Cartwright, J. K., Farmer, A. J., Padin, S., Myers, S. T., Bond, J. R., Contaldi, C. R., Pen, U., Prunet, S., Pogoyan, D., Carlstrom, J. E., Kovac, J., Leitch, E. M., Pryke, C., Halverson, N. W., Holzzapfel, W. L., Altamirano, P., Bronfman, L., Casassus, S., May, J., & Joy, M. 2003, *ApJ*, 591, 540
- Montroy, T. E., Ade, P. A. R., Bock, J. J., Bond, J. R., Borrill, J., Boscaleri, A., Cabella, P., Contaldi, C. R., Crill, B. P., de Bernardis, P., De Gasperis, G., de Oliveira-Costa, A., De Troia, G., di Stefano, G., Hivon, E., Jaffe, A. H., Jones, W. C., Kisner, T. S., Lange, A. E., MacTavish, C. J., Masi, S., Mauskopf, P. D., Melchiorri, A., Natoli, P., Netterfield, C. B., Pascale, E., Piacentini, F., Pogoyan, D., Polenta, G., Prunet, S., Ricciardi, S., Romeo, G., Ruhl, J. E., Santini, P., Tegmark, M., Veneziani, M., & Vittorio, N. 2006, *ApJ*, 647, 813
- Mukherjee, P. & Wang, Y. 2003, *ApJ*, 599, 1
- Pearson, T. J., Mason, B. S., Readhead, A. C. S., Shepherd, M. C., Sievers, J. L., Udomprasert, P. S., Cartwright, J. K., Farmer, A. J., Padin, S., Myers, S. T., Bond, J. R., Contaldi, C. R., Pen, U., Prunet, S., Pogoyan, D., Carlstrom, J. E., Kovac, J., Leitch, E. M., Pryke, C., Halverson, N. W., Holzzapfel, W. L., Altamirano, P., Bronfman, L., Casassus, S., May, J., & Joy, M. 2003, *ApJ*, 591, 556
- Peiris, H. V., Komatsu, E., Verde, L., Spergel, D. N., Bennett, C. L., Halpern, M., Hinshaw, G., Jarosik, N., Kogut, A., Limon, M., Meyer, S. S., Page, L., Tucker, G. S., Wollack, E., & Wright, E. L. 2003, *ApJS*, 148, 213
- Piacentini, F., Ade, P. A. R., Bock, J. J., Bond, J. R., Borrill, J., Boscaleri, A., Cabella, P., Contaldi, C. R., Crill, B. P., de Bernardis, P., De Gasperis, G., de Oliveira-Costa, A., De Troia, G., di Stefano, G., Hivon, E., Jaffe, A. H., Kisner, T. S., Jones, W. C., Lange, A. E., Masi, S., Mauskopf, P. D., MacTavish, C. J., Melchiorri, A., Montroy, T. E., Natoli, P., Netterfield, C. B., Pascale, E., Pogoyan, D., Polenta, G., Prunet, S., Ricciardi, S., Romeo, G., Ruhl, J. E., Santini, P., Tegmark, M., Veneziani, M., & Vittorio, N. 2006, *ApJ*, 647, 833
- QUaD Collaboration: P. Ade, Bock, J., Bowden, M., Brown, M. L., Cahill, G., Carlstrom, J. E., Castro, P. G., Church, S., Culverhouse, T., Friedman, R., Ganga, K., Gear, W. K., Hinderks, J., Kovac, J., Lange, A. E., Leitch, E., Melhuish, S. J., Murphy, J. A., Orlando, A., Schwarz, R., O'Sullivan, C., Piccirillo, L., Pryke, C., Rajguru, N., Rusholme, B., Taylor, A. N., Thompson, K. L., Wu, E. Y. S., & Zemicov, M. 2007, *ArXiv e-prints*, 705
- Readhead, A. C. S., Mason, B. S., Contaldi, C. R., Pearson, T. J., Bond, J. R., Myers, S. T., Padin, S., Sievers, J. L., Cartwright, J. K., Shepherd, M. C., Pogoyan, D., Prunet, S., Altamirano, P., Bustos, R., Bronfman, L., Casassus, S., Holzzapfel, W. L., May, J., Pen, U.-L., Torres, S., & Udomprasert, P. S. 2004a, *ApJ*, 609, 498
- Readhead, A. C. S., Myers, S. T., Pearson, T. J., Sievers, J. L., Mason, B. S., Contaldi, C. R., Bond, J. R., Bustos, R., Altamirano, P., Achermann, C., Bronfman, L., Carlstrom, J. E., Cartwright, J. K., Casassus, S., Dickinson, C., Holzzapfel, W. L., Kovac, J. M., Leitch, E. M., May, J., Padin, S., Pogoyan, D., Pospieszalski, M., Pryke, C., Reeves, R., Shepherd, M. C., & Torres, S. 2004b, *Science*, 306, 836
- Riess, A. G., Strolger, L., Tonry, J., Casertano, S., Ferguson, H. C., Mobasher, B., Challis, P., Filippenko, A. V., Jha, S., Li, W., Chornock, R., Kirshner, R. P., Leibundgut, B., Dickinson, M., Livio, M., Giavalisco, M., Steidel, C. C., Benítez, T., & Tsvetanov, Z. 2004, *ApJ*, 607, 665
- Riess, A. G., Strolger, L.-G., Casertano, S., Ferguson, H. C., Mobasher, B., Gold, B., Challis, P. J., Filippenko, A. V., Jha, S., Li, W., Tonry, J., Foley, R., Kirshner, R. P., Dickinson, M., MacDonald, E., Eisenstein, D., Livio, M., Younger, J., Xu, C., Dahlén, T., & Stern, D. 2007, *ApJ*, 659, 98
- Runyan, M. C., Ade, P. A. R., Bhatia, R. S., Bock, J. J., Daub, M. D., Goldstein, J. H., Haynes, C. V., Holzzapfel, W. L., Kuo, C. L., Lange, A. E., Leong, J., Lueker, M., Newcomb, M., Peterson, J. B., Reichardt, C., Ruhl, J., Sirbi, G., Torbet, E., Tucker, C., Turner, A. D., & Woolsey, D. 2003, *ApJS*, 149, 265
- Schlegel, D. J., Finkbeiner, D. P., & Davis, M. 1998, *ApJ*, 500, 525
- Scott, D. & White, M. 1999, *A&A*, 346, 1
- Seljak, U. 1996, *ApJ*, 463, 1
- Sievers, J. L., Achermann, C., Bond, J. R., Bronfman, L., Bustos, R., Contaldi, C. R., Dickinson, C., Ferreira, P. G., Jones, M. E., Lewis, A. M., Mason, B. S., May, J., Myers, S. T., Padin, S., Pearson, T. J., Pospieszalski, M., Readhead, A. C. S., Reeves, R., Taylor, A. C., & Torres, S. 2005, *ArXiv Astrophysics e-prints*
- Smith, K. M., Zahn, O., & Doré, O. 2007, *Phys. Rev. D*, 76, 043510

- Spergel, D. N., Bean, R., Dore, O., Nolta, M. R., Bennett, C. L., Hinshaw, G., Jarosik, N., Komatsu, E., Page, L., Peiris, H. V., Verde, L., Barnes, C., Halpern, M., Hill, R. S., Kogut, A., Limon, M., Meyer, S. S., Odegard, N., Tucker, G. S., Weiland, J. L., Wollack, E., & Wright, E. L. 2006, *ArXiv Astrophysics e-prints*
- Spergel, D. N., Verde, L., Peiris, H. V., Komatsu, E., Nolta, M. R., Bennett, C. L., Halpern, M., Hinshaw, G., Jarosik, N., Kogut, A., Limon, M., Meyer, S. S., Page, L., Tucker, G. S., Weiland, J. L., Wollack, E., & Wright, E. L. 2003, *ApJS*, 148, 175
- Subramanian, K., Seshadri, T. R., & Barrow, J. D. 2003, *MNRAS*, 344, L31
- Tegmark, M. 1997, *Phys. Rev. D*, 55, 5895
- Tegmark, M., Eisenstein, D. J., Strauss, M. A., Weinberg, D. H., Blanton, M. R., Frieman, J. A., Fukugita, M., Gunn, J. E., Hamilton, A. J. S., Knapp, G. R., Nichol, R. C., Ostriker, J. P., Padmanabhan, N., Percival, W. J., Schlegel, D. J., Schneider, D. P., Scoccimarro, R., Seljak, U., Seo, H.-J., Swanson, M., Szalay, A. S., Vogeley, M. S., Yoo, J., Zehavi, I., Abazajian, K., Anderson, S. F., Annis, J., Bahcall, N. A., Bassett, B., Berlind, A., Brinkmann, J., Budavari, T., Castander, F., Connolly, A., Csabai, I., Doi, M., Finkbeiner, D. P., Gillespie, B., Glazebrook, K., Hennessy, G. S., Hogg, D. W., Ivezić, Ž., Jain, B., Johnston, D., Kent, S., Lamb, D. Q., Lee, B. C., Lin, H., Loveday, J., Lupton, R. H., Munn, J. A., Pan, K., Park, C., Peoples, J., Pier, J. R., Pope, A., Richmond, M., Rockosi, C., Scranton, R., Sheth, R. K., Stebbins, A., Stoughton, C., Szapudi, I., Tucker, D. L., Berk, D. E. V., Yanny, B., & York, D. G. 2006, *Phys. Rev. D*, 74, 123507
- Tegmark, M., Strauss, M. A., Blanton, M. R., Abazajian, K., Dodelson, S., Sandvik, H., Wang, X., Weinberg, D. H., Zehavi, I., Bahcall, N. A., Hoyle, F., Schlegel, D., Scoccimarro, R., Vogeley, M. S., Berlind, A., Budavari, T., Connolly, A., Eisenstein, D. J., Finkbeiner, D., Frieman, J. A., Gunn, J. E., Hui, L., Jain, B., Johnston, D., Kent, S., Lin, H., Nakajima, R., Nichol, R. C., Ostriker, J. P., Pope, A., Scranton, R., Seljak, U., Sheth, R. K., Stebbins, A., Szalay, A. S., Szapudi, I., Xu, Y., Annis, J., Brinkmann, J., Burles, S., Castander, F. J., Csabai, I., Loveday, J., Doi, M., Fukugita, M., Gillespie, B., Hennessy, G., Hogg, D. W., Ivezić, Ž., Knapp, G. R., Lamb, D. Q., Lee, B. C., Lupton, R. H., McKay, T. A., Kunszt, P., Munn, J. A., O'Connell, L., Peoples, J., Pier, J. R., Richmond, M., Rockosi, C., Schneider, D. P., Stoughton, C., Tucker, D. L., vanden Berk, D. E., Yanny, B., & York, D. G. 2004, *Phys. Rev. D*, 69, 103501
- White, M., Hernquist, L., & Springel, V. 2002, *ApJ*, 579, 16
- White, M. & Majumdar, S. 2004, *ApJ*, 602, 565
- Wright, A. E., Griffith, M. R., Burke, B. F., & Ekers, R. D. 1994, *ApJS*, 91, 111
- Zhang, P., Pen, U., & Wang, B. 2002, *ApJ*, 577, 555